Revision 1

1   **AN EXPERIMENTAL CRYSTALLIZATION OF THE MACUSANI OBSIDIAN IN A**

2   **THERMAL GRADIENT WITH APPLICATIONS TO LITHIUM-RICH GRANITIC**

3   **PEGMATITES**

4   David London

5   dlondon@ou.edu

6   **Abstract**

7   Drilled cores of Macusani green obsidian pebbles from Peru were hydrated and melted above

8   their liquidus temperatures at 200 MPa to a single column ~ 4 cm in length and then undercooled

9   in a thermal gradient > 150°C along the length of the cores. Despite thousands of hours at

10   subliquidus temperatures, the crystallinity of the products ranged from ~ 30 vol.% to ~ 5 vol.%.

11   Mineral assemblages varied along the length of the cores but not in relation to the thermal

12   gradients in all cases. Oscillations in the abundances of plagioclase, K-feldspar, and quartz were

13   observed across the crystallization fronts and along the lengths of the cores. The originally

14   homogeneous melts became heterogeneous in response to crystallization and to thermal

15   gradients. Chemical gradients in the glasses included sharp boundary layer pile-up of F and B

16   adjacent to the crystallization fronts, as well as linear gradients among several of the elements

17   spanning the entire lengths of the melt columns. Values of molar K/(K+Na) in the glasses,

18   plotted as K*, varied positively with Si, inversely with Al and F, and positively with the domains

19   of K-feldspar that formed at maximum distance from the plagioclase-rich regions. Overall, the

20   results are marked by sharply bounded textural domains, by the spatial segregation of mineral

21   assemblages, by oscillations in mineral assemblages at multiple scales, and by monomineralic

22   crystal aggregates that are hallmarks of pegmatite bodies. Temperatures recorded by feldspars

23   closely approached the actual temperature gradient down to ~ 500°C, and the solvus on the alkali

Revision 1

24   feldspar join has been delineated for the first time by the simultaneous crystallization of feldspars

25   from an undercooled melt.

26   Key words: experimental petrology, granite, pegmatite, feldspar, thermometry

Introduction

28   Over the history of experimentation in igneous systems, only a handful of studies have attempted

29   to document the crystallization of melts in response to cooling, despite the fact that cooling is the

30   principal driver of crystallization in natural melts. Thermal models of thin granitic dikes that

31   form pegmatites predict that they would experience sharp thermal gradients from their margin to

32   center. The few experimental programs that have been meant to simulate the pegmatite-forming

33   environment, however, have been conducted at an isothermal state throughout the charges. This

34   study reports on the crystallization response of the Macusani obsidian (U.S. National Museum

35   specimens catalogued as #2143), a close analogue to the compositions of lithium-rich pegmatites

36   (Table 1), in thermal gradients that were meant to mimic those across half of a pegmatite dike

37   from margin to center. The principal contributions of these experiments include a validation of

38   the feldspar solvus algorithms to low, subsolidus temperatures, an experimentally determined

39   solvus for the alkali feldspars attained through the crystallization of undercooled melt at low

40   temperature, records of chemical gradients along and across the melt volumes, and

41   documentation of the spatial zonation of crystalline assemblages and their textures.

42   **Geological Context**

43   These experiments arise from the following observations, which served as the premise for the

44   approach:

Revision 1

45   (1) Pegmatites solidify by the fractional crystallization of granitic melts from the margins of

46   bodies to center (e.g., Cameron et al., 1949; Jahns, 1953a). Additional components of lithium,

47   boron, fluorine, and phosphorus that act as fluxes in the melt constitute less than a couple of

48   weight percent in total, even in the most fractionated of igneous bodies (e.g., Jahns and Ewing,

49   1977; Stilling et al., 2006). The rare-element pegmatites comprise far less than 1% of all

50   pegmatites of a given pegmatite group or district (Norton and Redden, 1990; Černý, 1991). The

51   vast majority are mineralogically ordinary granites close to their thermal minimum composition

52   (Norton, 1966).

53   (2) The outer zones of pegmatites possess surface nucleation textures including skeletal

54   intergrowths of quartz with tourmaline, beryl, albite, and K-feldspar (graphic granite),

55   prominently oriented unidirectional crystal growth inward, and radial aggregates. These textures

56   are indicative of crystal growth from a melt of high viscosity that is highly supersaturated with

57   respect to mineral-forming components as a result of a large magnitude of liquidus undercooling

58   prior to the onset of crystallization (e.g., London, 2008, 2009). The immediate contacts of

59   pegmatites, thick and thin, are marked by granophyric intergrowths, an igneous quench texture,

60   of quartz with plagioclase (London et al., 2020).

61   (3) Assemblages that can be reasonably construed as the products of hydrothermal

62   recrystallization of earlier-formed minerals constitute less than 5 volume percent of pegmatites,

63   even those that are rare-element rich (e.g., Heinrich, 1953; Jahns, 1953b). Miarolitic cavities,

64   which represent incontrovertible evidence for the evolution of an aqueous solution at the end of

65   consolidation of pegmatites, represent only a minute fraction (far less than 1%) of all granitic

66   pegmatites (e.g., Černý, 2000). In contrast, the crystallization of a haplogranite melt that is

67   saturated in H_2O (6.6 wt.%) at 200 MPa leads to an increase in volume of 21%, of which the

Revision 1

68   aqueous solution occupies 25% of the total volume (London, 2008). That calculation has been

69   confirmed by experiment (Figure 5 of London and Morgan, 2017). In that context, the absence of

70   miarolitic cavities in pegmatites and the lack of adjacent host rock alteration are significant

71   (Bowen, 1928).

72   (4) Primary solvus feldspars record temperatures of ~ 400°C along the margins to ~ 450°C at

73   centers of thin dikes (London et al., 2020, 2021). The cesium content of primary K-feldspars in

74   pegmatites serves as a measure of the extent to which the feldspars have preserved their original

75   igneous compositions. Rayleigh models based on the Cs content of the unaltered K-feldspars in

76   pegmatites reflect their crystallization from melt in the absence of an aqueous solution until the

77   ends stages of crystallization (London, 2022).

78   (5) Numerical simulations of conductive heat flow indicate that intrusive pegmatite bodies

79   should cool quickly to ~ 400°-450°C at their margins with the ingress of a sharp thermal gradient

80   from margin to center (e.g., London, 2008). The crystallization of the feldspars appears to keep

81   pace with the advance of an isotherm of ~ 400°C (London et al., 2019, 2020).

82   **Background**

83   At the inception of experimentation on rock-forming igneous systems, Bowen (1913) observed

84   that the products of melting crystalline aggregates were not reproducible by cooling liquids of

85   the same composition. In the plagioclase system, Bowen (1913) found that crystal-free melts had

86   to be cooled to temperatures well below the liquidus conditions observed in the crystalline

87   melting experiments, and many compositions failed to crystallize at all. He deduced that the

88   undercooled melts persisted metastably below their liquidus temperature because their high

89   viscosity impeded the nucleation of crystals. From that point on, liquidus experimentation

Revision 1

90   entailed thermally prograde (also known as forward-direction) experiments that involved the

91   melting of crystalline aggregates, or less commonly the forward-direction crystallization from

92   glasses. For the most part, these were partial melting experiments in which little or nothing

93   actually crystallized, yet the liquidus relations that were derived from them were related to the

94   crystallization of geologic melts upon cooling. Experiments in which silicate compositions were

95   fully melted above their liquidus temperatures, then cooled below the liquidus temperatures

96   (thermally retrograde or reverse-direction) to induce crystallization, were abandoned for decades.

97   The first significant attempts to quantify the crystallization response of high-silica melts as a

98   function of liquidus undercooling were conducted in the alkali feldspar system (Fenn, 1977) and

99   with synthetic granitic and granodioritic rock compositions (Swanson, 1977). Both authors

100   plotted crystal growth rates (the single largest dimension of a crystal grown entirely within melt

101   over the duration of an experiment) and crystal nucleation rates (actually, crystal density, the

102   number of crystals per unit volume as a function of the duration of an experiment) against the

103   magnitude of liquidus undercooling, ΔT. The magnitude of ΔT correlates with the magnitude of

104   the Gibbs Free Energy change of reaction for the crystallization of a chemical component of a

105   mineral from its components in the melt: $\Delta \bar{G}_{rxn} = \bar{G}_{i,crystal} - \bar{G}_{i,liquid}$ where i is the chemical

106   composition of a mineral-forming component, e.g., $i_{NaAlSi3O8}$. Values of $\Delta \bar{G}_{rxn}$ become

107   increasingly negative, favoring the formation of crystals, with increasing ΔT.

108   **Simulation Experiments**

109   Though Fenn (1977) and Swanson (1977) aimed to produce quantitative measures of

110   crystallization in felsic melts, they took the approach of simulating crystallization upon cooling,

111   and they related their results to the textures of igneous rocks that form at different rates of

112   cooling. They regarded their experiments, therefore, as simulations of the natural igneous

5

Revision 1

113   environment to a first approximation. The first experiment that was explicitly treated as a

114   simulation of a natural process of crystallization in a granitic composition, however, was

115   published by Wyllie (1963; reproduced as Figure 6 of London, 1992). He attributed that single

116   experiment to R.H. Jahns and C.W. Burnham. Jahns and Burnham never published the

117   experiment, nor did they provide details of it in any other publication. Jahns (1982) described it

118   as a perfect simulation and replication of the pegmatite-forming process following the Jahns-

119   Burnham (1969) model, though he did not depict or take credit for the experiment. Wyllie (1963)

120   attributed the same textural variations in two domains of the run product to a thermal gradient

121   across the capsule, not along its length.

122   London et al. (1989) approached experimentation with the Macusani obsidian, a rhyolitic glass

123   that is highly enriched in F, P, B, Li, Rb, and Cs (Table 1), in the same manner as did Fenn and

124   Swanson. Powdered Macusani glass was devitrified at 400°C and 200 MPa H_2O prior to

125   forward-direction melting steps. A succession of experiments led to a liquidus diagram (Figure

126   1) as functions of temperature and H_2O content of the experimental charge at 200 MPa total

127   pressure (nominally anhydrous[1] glass to H_2O-oversaturated). A subsequent suite of experiments

128   with powdered glass and variable H_2O content was run to temperatures above the liquidus

129   (determined in relation to the amount of added H_2O) to produce a homogeneous melt, then

130   cooled below the liquidus temperature. The majority of experiments entailed isobaric single-step

131   cooling (Figure 1), and the results were related to the initial magnitude of undercooling, ΔT, as a

132   function of the H_2O content of the experiment up to saturation (10-11 wt.% H_2O). The

133   relationship of crystallization to H_2O content was complex and unexpected: the nominally

134   anhydrous Macusani obsidian powder crystallized immediately and completely at run conditions,

[1] London et al. (2012) pointed out that powdered (micronized) starting materials adsorb from 1 to 4 wt% of their weight in H_2O from atmospheric moisture in the brief times they are exposed to air, even if stored under desiccation.

Revision 1

135   but as the content of H_2O added increased past 4 wt.%, no crystallization ensued until the

136   experiments were oversaturated in an aqueous solution[2]. In that state, crystallization occurred

137   solely by deposition along the capsule walls from the aqueous solution, and the melt remained

138   entirely crystal-free.

139   The H_2O-undersaturated powder experiments reproduced pegmatitic features in most respects,

140   whereas the initially H_2O-oversaturated experiments did not. Undersaturated experiments

141   recorded sequential crystallization, unidirectional solidification textures (UST), graphic feldspar-

142   quartz intergrowths, and sharp spatial zonation of mineral assemblages from margins to center of

143   the melt volumes. With crystallization in the vapor space, oversaturated experiments produced

144   euhedral crystals in a spatially random assemblage with voids between crystals in the spaces of

145   the aqueous solution. The texture resembled that of crystals found in miarolitic cavities of some

146   pegmatites (e.g., London, 2013). At comparable degrees of crystallization, the H_2O-

147   undersaturated melt showed progressive fractionation of the melt in terms of increasing

148   concentrations of incompatible and fluxing components, whereas the melt in H_2O-oversaturated

149   showed little or no fractionation at all (Table 8 of London et al., 1989).

150   In a similar study of the kinetics of crystallization upon liquidus undercooling of a hydrous

151   haplogranite liquid of minimum composition at 200 MPa H_2O, Evensen (2001) observed that

152   starting materials of glass powder crystallized partially but readily along the interface between

153   aqueous solution and melt, but identical replications with solid glass cores failed to

154   crystallize at all. The experimental study by Evensen (2001) and continued by London (2008)

155   entailed 275 experiments, but it was never published because its goal was to assess the intrinsic

---

[2] Swanson (1977) noted that the granitic composition failed to nucleate crystals for any combination of time and undercooling temperature with more than 3.5 wt% H_2O added to the charge (p. 969).

Revision 1

156   crystallization response of hydrous granitic liquid to cooling. The results turned out to be highly

157   extrinsic, determined by the experimental methods as much as by the composition and its

158   conditions. Results varied based on the starting state at the undercooling step, whether from

159   melted glass powder, devitrified and remelted glass powder, or melted glass core. Recently,

160   however, Devineau et al. (2020) have relied on seven undercooled experiments with granitic

161   powder to account for the textural crystallization of pegmatites.

162   The observations from the study of hydrous haplogranite powder versus cored glass (Evensen,

163   2001), therefore, led London and Morgan (2017) to replicated experiments with the Macusani

164   obsidian using solid glass cores instead of powders in order to produce a better simulation of a

165   natural magma. To improve the simulation, London and Morgan (2017) added powdered

166   amphibolite to one end of some capsules and completely surrounding some glass cores, such that

167   the glass cores were in contact with a rock that might be regarded as a natural host. As in the

168   study by Evensen (2001), London and Morgan (2017, p. 1025-1026) reported significant

169   differences between powdered and isothermal core glass experiments of otherwise identical

170   design. Their conclusion was that core experiments, which excluded a large quantity of air from

171   the run material, provided a three-dimensional volume in contrast to the flattened two-

172   dimensional products of powders, and which avoided possible contamination or other lab-

173   induced effects from grinding and adsorption of moisture or solvents, represented a better

174   simulation of the natural process of crystallization. The addition of amphibolite powder to one

175   end of a capsule served the purpose of initiating crystallization of the melt there, as if along the

176   contact of a likely host rock, which led to the spatial separation of mineral assemblages across

177   the melt volume. London and Morgan (2017) deemed powders as unsuitable starting materials if

178   the experimentation is meant to simulate a natural igneous process.

Revision 1

179   The simulation experiments that have been conducted to date were isothermal throughout their

180   volume following the undercooling step. To this extent they are not adequate replications of a

181   natural dike-forming melt that might crystallize in a thermal gradient from margins to center. A

182   few new experiments with solid cores of the Macusani obsidian have started to address this

183   deficiency.

184   **Methods**

185   **Experimental Method 1 (MAC 246 and 247)**

186   Cores of ~ 4-5 mm (L) by 2.5 mm (W) were drilled from an obsidian pebble of the Macusani

187   obsidian (USNM 2143) obtained from the U.S. National Museum of Natural History. The cores

188   were beveled slightly along their ends to prevent their edges from cutting the Au tubing, rinsed

189   in technical grade HF for 3 seconds to remove any traces of abrasives, then washed in

190   ultrafiltered deionized water. Eight cores in MAC 246, and six cores in MAC 247, totaling ~ 4

191   cm in length, were loaded into Au capsules along with ultrafiltered deionized water (Table 2),

192   frozen at the end with water, and sealed with a TIG DC arc welder. Capsules were checked for

193   leakage by heating to 100°C in air for 2 hrs. Capsules were pressurized to 198 MPa in water-

194   pressurized cold seal reaction vessels and taken up to temperature above the liquidus for the

195   composition. The final pressure was adjusted to 200 MPa at temperature with reference to a

196   Bourdon-tube gauge. The controller temperature was set to 800°C, which was measured by an

197   internal Chromel-Alumel thermocouple to be within 10°-15°C of that value at the hot end of the

198   capsule. The temperature measured by the thermocouple, which was within 8-10 mm of the core

199   at the cooler end of the capsule, was 755°C. The fugacity of O_2 in the experimental system,

200   previously calibrated with respect to the solubility of cassiterite in melt (Taylor and Wall, 1992),

201   was 1 log unit below NNO at pressure and temperatures, which resulted in a proportion of

Revision 1

202   Fe^{3+}/Fe^T of < 10% (Moore et al., 1995). Cores were preconditioned for 144 hrs. Based on a

203   control experiment quenched from the preconditioning step, this procedure was sufficient to

204   completely melt and homogenize the glass. Following the preconditioning step, the reaction

205   vessel was repositioned outward toward the cool end of the furnace, such that the thermocouple

206   temperature at the cool end of the capsule was read at 400°C or 450°C (Table 2). Because the

207   crimped end of the capsule created an 8-10 mm gap between the end of the thermocouple and the

208   end of the core, the likely temperatures at the cold end of the cores are taken as 410° and 460°C

209   respectively. The hot ends of the capsules in the final run position were calibrated prior to the

210   experiments with a thermocouple located where the hot end of the capsule would lie. That value

211   was 610°C (MAC 246) and 585°C (MAC 247) with an uncertainty of ± 15°C (Table 2) because

212   there was no thermocouple in place at the hot end during a run. End-to-end, the temperature

213   gradients were ~ 160°C along MAC 246 and ~ 185°C along MAC 247.

214   **Experimental Method 2 (MAC 244)**

215   Eight cores for MAC 244 were prepared as described above with 4 wt.% H_2O and run at a set

216   point temperature of 800°C at 200 MPa linking them into a single glass column ~ 4 cm long.

217   Prior calibrations of the furnace gradient put the hot end temperature at 785°C (set to 800°C,

218   read at thermocouple). The duration of the preconditioning of the core (96 hrs) was sufficient to

219   hydrate it without inducing crystallization at the cold end (verified by inspection). The run was

220   quenched, the cooler end of that experiment was cut off (glass examined optically for crystals),

221   and that end placed against powdered amphibolite plus water in an outer capsule (a total of 6

222   wt.% H_2O added and in hydrated glass). The inner Au capsule, in which the cores were hydrated,

223   prevented any chemical exchange between the melt core and the amphibolite except at the open

224   end. The MAC 244 run was reloaded with the vessel repositioned in the furnace such as to give

10

225   an initial temperature of 785°C (the liquidus temperature for a melt with 4 wt% H_2O is 750°C) at

226   the hot end ("T Hot", Figure 2) and 540°C at the "Read T Cold" end of the experiment (Figure 2)

227   to establish an initial gradient of 245°C along the length of the core. In contrast to MAC 246 and

228   MAC 247, in which the thermal gradient of the undercooled melt remained constant over

229   distance and time, MAC 244 was cooled in a stepwise fashion to simulate the loss of heat and

230   decreasing temperature of a pegmatite body in contact with a cold host (Figure 2). MAC 244 was

231   conducted for 2,064 hrs below the liquidus temperature. The cold end of the MAC 244 core was

232   at or near a glass-forming state throughout the experiment. The hot end of the core approached

233   the glass state, assuming that was at ~ 550°C (London and Morgan, 2017), after 1,000 hrs.

234   **Analytical Methods**

235   Electron beam microanalysis included backscattered electron imaging (BSE), energy-dispersive

236   x-ray analysis (EDXA) of rastered areas, and spot analyses of minerals and glasses by

237   wavelength-dispersive x-ray spectrometery (WDS) on CAMECA SX50 and SX100 instruments

238   at the University of Oklahoma. Imaging was conducted using 15 kV acceleration and 20 nA

239   sample current (measured at the Faraday cup). Analyses by WDS also were performed using 15

240   kV acceleration. Crystalline phases were analyzed using 20 nA current, a spot size of 2 μm, and

241   counting times of 30s on peak for major elements and 30-60s for minor and trace elements

242   yielding minimum detection levels of ~0.02-0.07 wt.% for all components except F (~0.23 wt.%

243   using a TAP diffractor) and B (~ 0.2-0.4 wt.% B_2O_3 using an LSM device with 2d = 200Å: e.g.,

244   Morgan, 2015). To further investigate the potential incorporation of boron, selected feldspars

245   were analyzed using 8 kV acceleration, and beam current of 20 nA, and 5 μm spot size; counting

246   times were 30s for Na and Al, 60s for Si, and 75s for K, Ca, and B yielding minimum detection

247   levels of 0.01 to 0.02 wt.% for all elements except B (0.15 wt.%). Following the protocols of

Revision 1

248   Morgan and London (1996, 2005a), glasses were analyzed using two beam conditions to

249   minimize the effects of alkali volatilization. Both conditions utilized 15 kV acceleration and a

250   defocused 20 μm spot size; a 2 nA beam current was first used for analyzing Na, Al, Si, K, and

251   Ca (30s counting times, Na and Al measured first and concurrently), followed by a second 40 nA

252   condition (30-60s counting times) for all other minor and trace elements. Minimum detection

253   levels for glasses were similar to those obtained for crystalline phases. EDXA-based x-ray beam-

254   scanned mapping of selected samples was performed by spectral imaging on the CAMECA

255   SX100 using a Thermo Ultra-Dry SDD and Noran System Seven automation. Images were

256   acquired into 1024 x 768 pixel arrays, using 15 kV acceleration and 20 nA sample current; maps

257   were acquired using 200-300 frames acquired at 200s per frame. Phase analysis on the maps was

258   performed using the COMPASS principal components analysis model within the Noran

259   automation.

260   Solvus temperatures were calculated for pairs of plagioclase and K-feldspar using the Margules-

261   corrected fits to the solvus by Elkins and Grove (1990) in the software package SOLVCALC

262   (Wen and Nekvasil, 1994). Feldspar pairings were between adjacent (touching) plagioclase and

263   K-feldspar crystals. The uncertainty associated with each analysis was set at 2 mol.% deviation

264   from the mean for each component in plagioclase and K-feldspar. Values as mole fractions were

265   input to the fourth decimal place in order to include the low An content of K-feldspar, which was

266   close to the detection limit for most of the analyses (Electronic Appendix I). Using that accuracy,

267   temperatures were calculated for 40 pairs of touching feldspars; among those, only 9 failed to

268   converge on a temperature for all three feldspar components.

269   **Crystallization in a Thermal Gradient**

270   **Textures and Mineralogy of MAC 246**

12

271   Figure 3 presents backscattered electron images of the core from MAC 246. A visual estimate

272   over the entire core from BSE imagery indicates that ~ 70 vol.% of the core remained as glass.

273   Segment 1 contained a sharply defined, very fine-grained vesicular border zone up to 125 μm

274   thick (Figure 3a) that consisted of an intergrowth of skeletal lamellar crystals too fine to analyze

275   individually. Energy-dispersive x-ray analyses of the region were consistent with mostly

276   plagioclase. The border zone was followed inwardly by a layer of skeletal K-feldspar, then

277   coarse plagioclase to 500 μm in length tipped with more potassic K-feldspar at the crystallization

278   front. The sharply coarse-grained layer with inward UST will be referred to here as a wall zone;

279   the mineralogy and textures of the two zones, border and wall, are characteristic of the same

280   units in the same structural position in zoned pegmatites (Cameron et al., 1949). Radial sprays of

281   micas, whose cores of zinnwaldite evolved to lepidolite at the rims, were encased within large

282   quartz crystals to 250 μm across (see London and Morgan, 2017, for analyses of similar

283   intergrowths). The quartz-mica intergrowths shown in Figure 3a appear to have truncated, and

284   hence preceded, the terminus of the wall zone. Vesiculation caused by crystallization created

285   vesicles that are immediately adjacent to the crystallization front (Figure 3a). The extent of

286   vesiculation along the entire core was proportional to the amount of crystallization. Segments 2

287   through 6 contained a few minute vesicles, and segments 7 and 8, which were nearly free of

288   crystals, were equally devoid of vesicles. Along the margin of segments 3 and 4, the border zone

289   was ~ 10-20 μm wide. Large skeletal crystals of K-feldspar-plagioclase intergrowth radiated off

290   of this surface (Figure 3b), and at the contact with the glass, single euhedral crystals of K-

291   feldspar with plagioclase formed patchy intergrowths that have been observed in prior

292   experiments with the obsidian. Quartz formed small anhedral crystals within the skeletal

293   branches of the K-feldspar intergrowth and in an association with blocky albite in domains

13

Revision 1

294   between branching K-feldspars. Skeletal sprays of micas dotted the glass; some were encased in

295   quartz overgrowths, and some not (Figure 3c). Segments 5 and 6 were similar in that the border

296   zone was practically gone, and the crystallization front consisted mostly of skeletal K-feldspar

297   with interstitial albite and small anhedral grains of quartz; quartz constituted less than 15 vol.%

298   of the intergrowth. Segments 7 and 8 were entirely vitreous except for traces of patchy feldspar

299   intergrowths along their margins. In the glass of segment 8, thin blades of a stannous iron oxide

300   (unique to this run) were present along with other thin skeletal crystals too narrow to analyze, but

301   which resembled micas (Figure 3d).

302   **Feldspar Solvus Thermometry in MAC 246**

303   Figure 4 plots the convergent three-component (An-Ab-Or) temperatures (solid diamonds)

304   derived from the solvus thermometry program SOLVCAL against position within the

305   experimental core. The average temperature among the three components that did not converge

306   within the assigned error is shown as gray squares. A black line denotes the probable temperature

307   profile over the length of the core as extrapolated between calibrations at the hot and the cold

308   ends (open diamonds). The temperature of the hot end carried a larger uncertainty because there

309   was no thermocouple to record it. The uncertainty at the cold end was ~ 5°C. The liquidus

310   temperature of the Macusani obsidian containing 6 wt.% H_2O at 200 MPa (dotted line) is 725°C

311   (London et al., 1989). Upon positioning the vessel outward for the duration of the run, the

312   resultant instantaneous liquidus undercooling of melt (ΔT) varied from ~ 115°C at the hot end to

313   ~ 235°C at the cold end.

314   The calculated solvus temperatures in MAC 246 exhibit scatter but generally conform to the

315   decreasing temperature profile across the melt column. For all feldspar components in

316   plagioclase and K-feldspar, the convergence was better at low temperature than at the high end.

14

317   Many of the calculated temperatures for the Ab and An components are identical, and the

318   equilibration temperatures of the Ab and An components of the feldspars more closely

319   approached the temperature profile than did Or. The average calculated temperatures for the Or

320   component of K-feldspar exhibited an increasing deviation from the thermal profile of the

321   experiment with increasing temperature, which likely accounts for many of the convergent

322   values to deviate from the thermal profile along the capsule.

323   Figure 5 traces the feldspar solvus as functions of temperature versus mole fraction of Or

324   component in albite and K-feldspar for the convergent pairs only. It is the first known depiction

325   of the alkali feldspar solvus as derived by the simultaneous crystallization of feldspar pairs from

326   hydrous melt in response to cooling. The compositions of K-feldspar in MAC 246 lie on the

327   binary join between Ab and Or. The compositions of albite lie off of the join by an average of ~

328   5 mol.% An component (Electronic Appendix 1). Also shown on Figure 5 are the locations of the

329   solvus curve as calculated at 500°C and 600°C from the Margules mixing model of Elkins and

330   Grove (1990) as incorporated by Wen and Nekavasil (1994) into SOLVCALC. The calculated

331   solvus for albitic plagioclase is projected to the Ab-Or join from the An apex in the ternary

332   feldspar system through the solvus locations at 500°C and 600°C at An_{05}. Figure 5 illustrates the

333   correspondence between the calculated experimental temperatures and the calculated position of

334   the solvus in relation to albitic plagioclase and K-feldspar. For both feldspars, deviations of the

335   experimental data from the calculated solvus position increased with increasing temperature in

336   the direction of an increased Ab component. The K-feldspars contained up to half a weight

337   percent of Rb_2O, and both feldspars contained upwards of 0.5 wt.% P_2O_5 (Electronic Appendix

338   I). Both components, which were omitted from the solvus calculations, might have been

339   sufficient to influence the solvus solutions.

Revision 1

The Chemical Composition of Glass in MAC 246

340

341   The Macusani obsidian is notably homogeneous (e.g., London et al., 1988), and the

342   preconditioning step of melting insures that any minute crystals (except andalusite) or other

343   potential variations in composition are eliminated. Over the length of the glass column in MAC

344   246, however, gradients were observed among several of the components measured (Electronic

345   Appendix II). In Figure 6, thin dashed horizontal lines convey the initial elemental concentration

346   or elemental ratio in atoms per 8 oxygens for a melt of the Macusani obsidian containing 5 wt.%

347   H_2O. Vertical arrows in Figure 6 show the extent to which elements or ratios increased or

348   decreased over their values in the starting hydrated obsidian. Data are regressed to a linear fit.

349   Deviations along the length of profiles arise from the uneven distribution of crystal clusters along

350   the margins of the core and their consequent chemical fractionation of adjacent melt. From cold

351   to hot end, Si increased by 3% apfu based on 8 oxygens, and Al decreased by 7% Al apfu. Boron

352   decreased by 51% B apfu and phosphorus by 17% P apfu over the same distance. Fluorine,

353   however, fell by more than half, from 0.545 to 0.247 F apfu. The ratio of Rb/K fell 60% from the

354   cold to hot end, but all measured values were greater than the initial ratio in the Macusani

355   obsidian. The ratio of K to Na, measured as K*, apfu K/(K +Na), varied from 0.274 at the cold

356   end to 0.334 at the hot end, an increase of 18%.

Textures and Mineralogy of MAC 247

357

358   Figure 7 depicts representative backscattered electron images of the core. A visual estimate over

359   the entire core from BSE imagery indicated that ~ 95 vol.% of the core remained as glass. In

360   segment 1 at the cold end (Figure 7a), a thin vesicular border zone ~ 40 μm wide consisted of a

361   skeletal intergrowth of too fine to resolve, but EDXA are consistent with mostly plagioclase and

362   subordinate dendritic K-feldspar. A wall zone ensued with skeletal K-feldspar crystals up to 400

16

Revision 1

363   μm in length, followed by a layer of coarsely crystalline blocky plagioclase and quartz. A few

364   radial clusters of mica were isolated in the glass. Segment 2 contained but one small cluster of

365   crystals that repeated the plagioclase-rich border zone and the skeletal K-feldspar wall zone upon

366   it. The curving trace of a crack in the glass was delineated by a mica-quartz intergrowth (Figure

367   7b). The margins of segments 3 and 4 were lined with a monophase layer of petalite ($LiAlSi_4O_{10}$)

368   crystals ~ 20 μm in size with traces of skeletal K-feldspar at their junctions (Figure 8c).

369   Otherwise, no feldspars or micas were present in the segments. Segment 5 was all glass except

370   for a few minute dispersed crystals of mica (Figure 7d). Segment 6 at the hot end presented a

371   fine-grained margin of plagioclase, followed inwardly by a mostly crystal-free zone dotted with

372   micas, then a few clusters of radial feldspar and exceedingly fine-grained crystals that resembled

373   micas dispersed in the "glass" (Figure 7e). Small vesicles were present in the crystal-bearing

374   "glass".

375   **The Chemical Composition of Glass in MAC 247**

376   The chemical attributes of the glass are displayed in Figure 8 and Electronic Appendix III. As in

377   MAC 246, Si increased and Al apfu and ASI both decreased from cold to hot ends. Boron and

378   phosphorus showed no significant variation across the glass, but F was highly enriched adjacent

379   to the crystal front in segment 1 at the cold end. Within the same glass region, values of K* fell

380   well below the initial ratio, and beyond segment 2, K* values exceeded the initial ratio. The glass

381   was, therefore, more sodic where albite was most abundant in the adjacent crystalline zone, and

382   more potassic where K-feldspar was the predominant feldspar (though the fraction of

383   crystallization was minute toward the hot end).

384   **Textures and Mineralogy of MAC 244**

17

Revision 1

385   Figure 9 shows five composite BSE images of the 4-cm long experiment that was conducted

386   with decreasing temperature with time along its thermal gradient (Figure 2). A polyphase

387   crystallization front with mineralogically distinct domains occupied ~ 15 vol.% of the total core

388   but did not surround the margins of the core completely or uniformly; the remaining 85 vol.% of

389   the core was non-vesicular glass. Crystallization occurred along both ends of the composite core,

390   decreasing toward the central segments 4 and 5. End segments 1 and 8 contained ~ 10 vol.% of a

391   mineral dispersed through the glass that was too fine-grained for EMPA (labeled "glass" in

392   Figure 9). In its morphology and BSE intensity, the dispersed crystalline phase resembled mica,

393   but analyses of "glass" in these segments showed an increase in Si and a decrease in Al in this

394   region. Minute vesicles were attached to many grains of the dispersed mineral. Segment 1 was

395   likely in the glass state throughout its cooling. It possessed an exceedingly fine-grained border of

396   plagioclase and quartz (Figure 9a). Segment 8 (Figure 9e) at the hot end was texturally similar to

397   segment 1 despite its higher run temperatures from 785°C to 480°C). It presented a

398   mineralogically complex border zone with three oscillations of layers rich in K-feldspar and of

399   plagioclase plus quartz. Figure 10a illustrates the nature of the mineralogical variations both

400   across and along the crystallization front. A layered sequence dominated by K-feldspar with

401   lesser plagioclase plus quartz evolved to the opposite proportionality, dominated by plagioclase

402   plus quartz, from the margin inward and toward the end of the segment. The detailed mineralogy

403   at the end of segment 8 is revealed as a phase map based on a composite set of elemental x-ray

404   images of the area (Figure 10b). The glass in segment 2 contained dispersed crystals of skeletal

405   radial zinnwaldite included within quartz, and the same micas occurred in segment 3 but without

406   quartz (Figure 9b). Segment 5 contained a curved crystal-bordered crack that resembled similar

407   crystalline threads in the isothermal core experiments described in London and Morgan (2017),

Revision 1

408   and which they attributed to crystallization along fractures that developed on the cooling cycle of

409   experiments. Crystallization along the margins of segments 4 and 5 began with an exceedingly

410   fine-grained border zone dominated by plagioclase with minor mica, followed inwardly by a

411   graphic K-feldspar-quartz intergrowth, and terminated inwardly by a monophase layer of K-

412   feldspar at the melt interface (Figure 10d).

413   The compositions of entirely crystalline portions were analyzed by EDXA in 50 X 50 μm scan

414   areas, and their compositions were recast as CIPW norms. Within each of the eight core

415   segments, the crystallization front was divided into two domains based on texture: an

416   exceedingly fine-grained and finely vesicular border zone adjacent to the interface with the Au

417   tube, and a coarser wall zone displaying unidirectional crystal growth inward at the

418   crystallization front.

419   Figure 11 presents normative mineral variation diagrams along the length of the core for the

420   border and wall zones of the crystallization front. In the border and wall zones, normative quartz

421   decreased from ~ 25 wt.% at the cold end to ~ 20 wt.% at the hot end, as compared to 35.7 wt.%

422   CIPW normative quartz in the starting Macusani obsidian. Oscillations in normative albite and

423   orthoclase occurred at the scale of millimeters along the length of the border zone, and K-

424   feldspar was predominant in the central segments. The wall zone presented oscillations between

425   quartz and albite at the scale of millimeters along its length, and the same prominently potassic

426   region in the central segments. The normative corundum component of the CIPW norms, which

427   was contained as a component of mica, varied irregularly from ~ 1 to 4 wt.% depending on

428   whether a mica happened to be included in the analyzed area[3]. A relatively constant normative

---

[3] CIPW normative analyses do not include lithium, which would be expressed as a lithium aluminosilicate. As a
result, CIPW norms of Li-rich compositions overestimate the quartz and corundum components. For phosphorus-

Revision 1

429   hypersthene component (~ 1.4 wt.%) mirrored that of the starting obsidian, and was hosted as the

430   ferrous component of the micas.

The Chemical Composition of Glass in MAC 244

432   The glass portion of MAC 244 was analyzed with two different transects: at the center line along

433   the length of the core, and transects across each core segment (Electronic Appendix IV). Points

434   were picked by hand where necessitated by crystals, but crystals were unavoidable in the "glass"

435   domains of segments 1 and 8.

436   Figure 12 displays five chemical attributes of the glass along its length. Silicon was elevated

437   along the length of the glass core relative to the starting composition, a result that was dictated

438   by the low normative quartz component of the crystalline margins. The Si content of the glass,

439   however, increased within both end segments 1 and 8 of the core, and Al decreased in the same

440   volume (Figure 12a). Those variations implied that the finely divided crystalline material was

441   quartz, however as noted above, the morphology and BSE intensity of that crystalline material is

442   more akin to mica. The vitreous domains of cores 2-7, however, were free of crystals except for a

443   few large mica-quartz aggregates that were avoided. Potassium and K* increased from both ends

444   toward the center of the glass column, where the normative K-feldspar component of the

445   crystalline margins also attained a maximum and where the fraction of crystallization at the

446   margins was at a minimum along the length of the core. In Figure 12b, boron and phosphorus

447   were relatively unchanged from their starting concentrations and no gradients in their

448   concentrations were evident along the length of the glass transect. Fluorine, however, exhibited

---

rich compositions like the Macusani obsidian, CIPW norms also overestimate the apatite component, while the anorthite component typically becomes a negative value.

Revision 1

449   spikes in cores 2 and 7, which were the first fully vitreous domains inward from the more

450   extensively crystallized end segments.

451   Figure 13 plots a transect (yellow line in Figure 11) across the glass of segment 6 beginning at

452   the crystalline margin. A pronounced enrichment of B and F was evident near the crystallization

453   front. The concentration profile for P was flat, as it was in most other analyses of the glasses.

454   Though the value of K* was elevated above the starting composition in this segment, there was

455   no correlation between K* and F. Other transverse analyses were similar where a crystallization

456   front was present at the margin. No compositional gradients were found where crystals were

457   absent along the margins.

Discussion of Results

459   **A Comparison of Experimental Methods and Results**

460   Three experimental programs with the Macusani obsidian at 200 MPa (London et al, 1989;

461   London and Morgan, 2017, and this study) shared similarities, which might be construed as

462   intrinsic to the composition of the obsidian, and differences based on the experimental method.

463   These results with the Macusani obsidian have been consistently observed in all experiments:

464   (1) incipient crystallization at the margins produced a very fine-grained border zone dominated

465   by plagioclase and lesser quartz. The An content of plagioclase fell from margin ($\sim An_{08-12}$) to

466   center ($\sim An_{02-05}$).

467   (2) Inward of the border zone, a wall zone of coarse patchy or graphic intergrowth of K-feldspar

468   with albite or with quartz that exhibited unidirectional solidification texture formed elongate

469   crystals pointing toward the remaining melt pools. All crystalline phases coarsened by a factor of

470    $\sim 10^2$ from margin to melt center.

21

Revision 1

471   (3) Quartz formed overgrowths on the feldspar crystallization front and isolated crystals of

472   quartz and quartz plus mica in the central domains of melt pools. Micas were present throughout

473   the experiments, but they were abundant only in compositions with > 6 wt.% H_2O added (core

474   experiments only), or in which the H_2O content of melt increased beyond this value by the

475   fractional crystallization of feldspars and quartz along the margins.

476   To this extent, all three experimental programs replicated the spatial distributions of minerals and

477   textures found in the vast majority of common granitic pegmatites that possess simple zonation,

478   from plagioclase-quartz $\rightarrow$ K-feldspar $\rightarrow$ quartz $\pm$ mica (Cameron et al., 1949).

479   ***Crystallinity, undercooling, and H$_2$O content***.

480   The relationships among ΔT and H_2O content on crystallization, vesiculation of the melt, the

481   delay in crystal nucleation and growth, and the spatial distributions of the feldspars were

482   different among the three studies cited here. These differences are primarily a function of the

483   methods used.

484   The anhydrous obsidian powder crystallized immediately and completely upon approach to run

485   conditions (700°-800°C, 200 MPa), but crystallization decreased with increasing H_2O content of

486   the melt, and crystallization ceased abruptly beyond 4 wt% H_2O (London et al., 1989). In

487   contrast, anhydrous obsidian cores did not crystallize at all; crystallinity increased principally as

488   a non-linear function of time and liquidus undercooling (Figure 11 of London and Morgan,

489   2017). Though crystallization increased when H_2O was added, there was no correlation between

490   the percentage of crystallization and the initial H_2O content added to the charges (Figure 12 of

491   London and Morgan, 2017). At comparable compositions and undercooling, the experiments

492   presented here showed far less crystallization than in the isothermal core results over longer run

Revision 1

493   durations. Portions of MAC 244, 246, and 247 that were held above 500°C for at least 1,000

494   hours produced almost no crystallization, whereas isothermal core experiments of similar

495   temperature, duration, and H_2O content crystallized abundantly.

496   *Vesiculation*. Vesicles were absent along the crystallization fronts in powder experiments,

497   whereas vesicles were abundant at that interface in solid core runs. A continuous crystallization

498   front completely surrounded the margins of the cores in the isothermal experiments, whereas

499   crystal clusters in powder experiments left melt in contact with the precious metal tubing. The

500   entrapment of vesicles, therefore, appears to have been a function of the experimental geometry:

501   flattened charges (powder) with melt in contact with tubing allowed H_2O to diffuse out of melt

502   into the space around the melt body. Solidification fronts around cores appear to have inhibited

503   that process, leading to the nucleation and retention of aqueous bubbles at the crystallization

504   fronts.

505   The powder experiments, especially those of low initial H_2O content, trapped abundant bubbles

506   of air upon sintering, and air bubbles persisted throughout the runs. Air bubbles persist in viscous

507   melts because although nitrogen is highly compressible, it is almost completely insoluble in

508   silicic melts at elevated pressures (Mysen et al., 2008; London et al., 2012a). As a result, many

509   such experiments are vapor saturated regardless of their H_2O content, and the solubility of H_2O

510   in the air bubbles increases with the concentration of H_2O added. Figure 2 of Burnham and Jahns

511   (1962) illustrated the same trends in bubble entrapment in a series of three experiments, the first

512   nearly opaque with air bubbles at low H_2O content, culminating in nearly vesicle-free transparent

513   glass at high H_2O content. This observation is relevant to the proper interpretation of

514   experimental products: it is a fact that powder starting materials of high silica content trap and

Revision 1

515   retain air bubbles at moderate pressures (several hundred MPa); hence, they are vapor-saturated

516   whether the bulk composition is hydrous or not and H_2O-saturated or not.

517   In a geological context, the crystallization of highly undercooled and viscous melts should trap

518   abundant vesicles upon crystallization if the melts are indeed saturated in H_2O, as Bowen (1928,

519   p. 294) observed:

520   *"…deep bodies have sent dikes into surrounding rocks at all stages of their careers and these*

521   *dikes are often, at least at their margins, aphanitic or glassy. They have thus crystallized so*

522   *rapidly that if the liquid were vesicular the aphanite would be vesicular as well. Yet vesicular*

523   *dikes or dike selvages are exceedingly rare and are apparently always found in association with*

524   *flows which indicate for them a shallow depth… It is very much to be doubted, therefore, that*

525   *any process which involves vesiculation can be the principal or even an important process in*

526   *igneous differentiation. But even on the supposition that vesiculation is a common condition in*

527   *deep-seated magma and that for some reason its evidence is concealed from us, the quantitative*

528   *adequacy of the process is seriously in doubt."*

529   ***Sequential versus simultaneous crystallization***. In the powder experiments (London et al.,

530   1989), crystallization from margins toward melt ensued with a single episode of sequential

531   crystallization as described above. In the isothermal core experiments (London and Morgan,

532   2017), feldspar-dominant assemblages formed along the margins while quartz or quartz-mica

533   intergrowths precipitated as isolated crystals in the centers of melt pools, as was the case in this

534   study. The crystallization of feldspar-rich and quartz-rich domains appears to have been partly

535   simultaneous (e.g., as in Figure 3), much as Jahns (1982) suggested for pegmatites, but not by

536   the mechanism that he proposed. At the undercooled state of these experiments, feldspars

537   exhibited a propensity for nucleation along the marginal surfaces of the melt, irrespective of the

Revision 1

538   capsule, aqueous solution, or rock in contact with melt, whereas quartz nucleated

539   homogeneously within the melt. Neither vesicles nor rare inherited phenocrysts of andalusite in

540   the obsidian fostered crystal nucleation within the melt in any of the experiments.

541   In the isothermal core experiments (London and Morgan, 2017), the addition of powdered

542   amphibolite to one end of the capsule led to a marked end-to-end segregation of minerals:

543   plagioclase plus quartz precipitated adjacent to amphibolite, and K-feldspar formed at the

544   opposite end. London and Morgan (2017) cited the identical compositions of first-formed

545   plagioclase in experiments (powder and core) without amphibolite as evidence that the locus of

546   incipient crystallization along the interface with amphibolite was not the result of chemical

547   contamination of the adjacent melt. The two mineralogical domains at the ends of cores

548   constituted the complementary portions of a single assemblage, and the feldspars were close to

549   thermal (chemical) equilibrium despite having crystallized hundreds of degrees below their

550   liquidus temperatures. London and Morgan (2017) inferred that the incipient crystallization of

551   plagioclase plus quartz along the amphibolite induced the crystallization of K-feldspar at the

552   opposite end of the melt column based on the clearly sequential nature of these two feldspars in

553   the powder experiments. In that case, the two components of the assemblage would have been

554   nearly simultaneous, but not exactly, one as a matter of cause, the other an effect.

555   In this study, only MAC 244 produced enough crystallization over its length to allow any

556   comparison. The notable feature of MAC 244 is the concentration of K-feldspar in the central

557   core segments, and a corresponding increase in K and K* of glass in the same region. Following

558   from the logic of London and Morgan (2017), that result would be interpreted in the same way:

559   after the initial crystallization of plagioclase-richer domains at the ends of MAC 244, enrichment

25

Revision 1

560   of the melt in K occurred in opposite directions toward the center, where K-feldspar was mostly

561   deposited.

562   The spatial segregation of co-crystallizing minerals as seen in both sets of core experiments

563   addresses a fundamental misunderstanding of pegmatite zonation. That is, aggregates of one or

564   two minerals, for example monominerallic crystallization fronts of petalite in PEG 46 (London

565   and Morgan, 2017) and here in MAC 247 (Figure 7c), have historically been interpreted as

566   hydrothermal deposits because any one- or two-phase crystalline domain is far from the

567   composition of the granite minimum. What these experiments reveal is that the various parts of

568   any given assemblage can and do crystallize simultaneously in separate regions of the melt body,

569   thereby preserving a near-minimum assemblage in spatially separate mineralogical domains.

570   The observed sequences of crystallization among plagioclase, K-feldspar, and quartz can be

571   rationalized in relation to the Gibbs Free Energy change attending their crystallization from melt

572   (the parameter $\Delta\bar{G}_{rxn}$ as defined above). At a highly undercooled state of the melt, the

573   crystallization of anorthite liberates more thermal energy per mole than K-feldspar, and K-

574   feldspar more than albite (Table 3). The feldspars release far more energy than does quartz on an

575   equimolar Si_4O_8 basis. In the absence of Ca, K-feldspar would be expected as the first-formed

576   crystalline phase based on the data of Table 3, as was observed in the experiments of London

577   (1999) and Evensen (2001). When Ca is present even in small amounts, the first-formed phase is

578   the most calcic plagioclase that the system can produce because the An component of plagioclase

579   releases a substantial quantity of heat from the melt (Table 3). From that An-rich composition

580   along the margins of charges, feldspars evolve with isothermal cooling to the final composition

581   of solvus pairs (Figure 2 of London, 2014b). The same evolutionary trends of feldspars are

582   typical of zoned pegmatites (Cameron et al., 1949; London et al., 2012b, 2020, 2021).

26

Revision 1

583   *Oscillatory crystalline assemblages*. Crystallization in the powder and isothermal core

584   experiments produced one sequential episode of a ternary phase assemblage – plagioclase, K-

585   feldspar, quartz, in that order – before crystallization ceased. In Ca-absent haplogranite minimum

586   compositions, the single sequential episode of crystallization produced K-feldspar, plagioclase,

587   then quartz (London, 1999; Evensen, 2001). Those differences in the mineralogical sequence can

588   be rationalized by the data of Table 3, whereby the first-formed feldspar should be K-feldspar in

589   highly undercooled, Ca-free melts, but plagioclase when the melt contains a small fraction of Ca.

590   The normative mineral proportions and oscillations along the length of MAC 244 are remarkably

591   similar to the modal oscillations in the texturally complex Swamp dike from Ramona, California

592   (Figure 14). The normative quartz component of the feldspathic portions of MAC 244 is ~ 20-

593   25%, similar to its modal abundance in the footwall section of the Swamp dike, which

594   crystallized before most of the overlying pegmatite (London et al., 2012b). Those low quartz

595   contents of the outer portions of experiments and early footwall portions of a natural pegmatite

596   required that complementary quartz-rich portions of crystallization should follow sequentially in

597   the centers of pegmatite bodies.

598   **Metastable Persistence of Melt**

599   A notable feature of these experiments, like those from prior studies (e.g., Swanson, 1977; Fenn,

600   1977, 1986; London et al., 1989; Evensen, 2001; London and Morgan, 2017), is that

601   crystallization began but ceased over long durations in melts that remained highly undercooled,

602   hence metastably supersaturated with respect to the equilibrium state of the system. Morgan and

603   London (2005b) observed (but did not report) that the magnitudes of nucleation delay (time) and

604   liquidus undercooling (ΔT) that were necessary to initiate crystallization increased as bulk

605   compositions shifted from near the Or apex of the Ab-Or-Qz system toward the minimum

27

606   composition at 200 MPa. Fractionation attending liquidus undercooling within a single melt

607   composition could be expected to behave similarly, which would mean that crystallization would

608   cease as the composition of melt migrated toward the liquidus until sufficient undercooling

609   restarted it.

610   The metastable persistence of melt of flux-poor hydrous haplogranite compositions (Swanson,

611   1977; Evensen, 2001) and of flux-rich Macusani obsidian on the duration of months at

612   temperatures in the range of 450°-500°C is relevant to the cooling of thin pegmatite-forming

613   dikes. Dikes of 1 to 2 meters thickness have been modeled to cool to this temperature range at

614   their centers in days to weeks (e.g., London et al., 2012b, 2020, 2021). Feldspar solvus

615   temperatures from the pegmatites recorded nearly isothermal crystallization at $\sim 400° \pm 15°C$

616   across their width (London et al., 2020, 2021). If the crystallization of feldspars in these

617   pegmatites was coincident with the ingress of the cooling front, then the pegmatite bodies would

618   have had to have begun their crystallization almost immediately upon emplacement, and the

619   crystallization front would have had to have advanced at the rate of centimeters per day. Two

620   hypotheses are immediately apparent to account for this disparity between the long delay of

621   crystal nucleation and growth in experiments and the thermal models that predict rapid cooling

622   and crystallization at the temperatures recorded by the feldspars in pegmatites: (1) the

623   experiments are not an adequate simulation of the natural environment, or (2) feldspar

624   crystallization in the pegmatites commenced after the cooling front of $\sim 400°-450°C$ reached the

625   dike center.

626   In the latter case, the crystallization of a dike would have ensued from glass, but the rate of

627   cooling would have been much slower from that temperature, the duration of crystallization

628   longer, and the temperatures would be nearly uniform across the body of melt (see examples in

28

629   Chapter 16 of London, 2008). Skeletal habits and strongly anisotropic UST of highly elongate

630   crystals found in pegmatites are akin to spherulites that crystallize in obsidian. The skeletal

631   unidirectional intergrowth of feldspar and quartz in graphic granite (Figure 15), the defining

632   texture of pegmatites that is also the only texture found in pegmatites that is not also present in

633   hydrothermal veins[4], is a similar one-dimensional linear growth pattern that, like spherulites,

634   arises from a growth medium of high viscosity (London, 2008, 2009). In the case of graphic

635   granite, the high viscosity of the melt impedes the diffusion of excess silica away from the

636   interface, which leads to local saturation in quartz in troughs along the feldspar surface (Fenn,

637   1986). High viscosity of the melt also inhibits the lateral diffusion of high field strength ions

638   (e.g., Si, Al) along the crystal front that is necessary to promote the two-dimensional expansion

639   of the crystal surface to form large, single crystals (London, 2008, 2009). In most pegmatites, the

640   graphic granite intergrowth begins with exceedingly fine-grained blebs of quartz in feldspar

641   (Figure 15b) that coarsen inwardly to monophase K-feldspar crystals in massive quartz (Figure

642   15a), either because the rate of advance of the K-feldspar crystal slows, or because the diffusivity

643   of ions along its growth surface increases (London, 2008, 2009). Though Fenn (1986) speculated

644   that an aqueous solution might be implicated in the formation of graphic granite, London (2008,

645   2009) concluded that the growth medium for graphic intergrowths must be a highly viscous

646   medium for the reasons given above, from Fenn's (1986) work, and from hundreds of H_2O-

647   undersaturated experiments with the Macusani obsidian and other granitic compositions that

648   yielded graphic intergrowths. London (2018) presented experimental evidence in which the

649   simultaneous crystallization of feldspar and quartz from a highly supersaturated aqueous solution

[4] Other textures found in pegmatites including unidirectional solidification from the margins, spatial zonation of mineral assemblages, layered assemblages, and increasing crystal size from margins to center are present in hydrothermal veins. Graphic mineral intergrowths are not found in hydrothermal veins because the intergrowth hinges upon high viscosity and low ionic diffusivity through its growth medium.

650   that was generated via undercooling of the Macusani obsidian produced a feldspar-quartz

651   assemblage of euhedral crystals, not in a graphic intergrowth.

652   **Feldspar Solvus Thermometry at Low Temperatures**

653   London et al. (2020) noted that the experiments on which feldspar thermometry is based were

654   performed at temperatures hundreds of degrees higher than the temperatures at which

655   experiments such as these were conducted. All of the prior experimental calibrations of the alkali

656   feldspar solvus entailed the subsolidus, forward direction recrystallization of starting crystalline

657   compositions or glasses; none were crystallized from an undercooled melt. Fuhrman and

658   Lindsley (1988) and Parsons et al. (2009) cautioned that the solvus method becomes highly

659   inaccurate toward the alkali feldspar join of the system because of the steep slope of the solvus

660   with respect to temperature at low anorthite content of the feldspars. The anorthite content of

661   feldspars produced in these experiments, however, is so low (Electronic Appendix I) that their

662   compositions are nearly binary on the alkali feldspar side.

663   London and Morgan (2017) reported that albite-K-feldspar pairs synthesized at the margins of

664   melt pools consistently gave convergent solvus temperatures that were within $25° \pm 10°C$ of the

665   actual run temperature down to 500°C. They cited this correlation as evidence that the solutions

666   to the solvus surface were sufficientlly accurate, even at low temperature and low anorthite

667   content of the feldspars, as to be useful for thermometry in pegmatites if it could be

668   demonstrated that the feldspars had preserved their igneous compositions. They noted, however,

669   that the discrepancies between calculated and measured temperature were always on the high

670   side of the run state, even for forward-direction experiments that never achieved the calculated

671   temperature. London et al. (2020) concluded that in regard to the energy released by

30

Revision 1

672   crystallization to approach an equilibrium state, close is close enough for the feldspars, and they

673   approach that chemical equilibrium from a fictive higher temperature.

674   The data from MAC 246 and from London and Morgan (2017) demonstrate that the feldspars

675   attain their near-equilibrium compositions even following instantaneous cooling by hundreds of

676   degrees below their liquidus temperatures and from melts of high viscosity that might have been

677   glass. Rapid equilibration of feldspars at such low temperatures requires rapid diffusion of the

678   alkalis through melt or glass. Acosta-Vigil et al. (2012) and Morgan and London (2005b)

679   documented that the diffusion of alkalis through hydrous haplogranite melt and glass is rapid and

680   coordinated down to 515°C at 200 MPa, which would facilitate the equilibration of the feldspars

681   at low temperatures through an exceedingly viscous growth medium. The experimental data base

682   that is now available validates the conclusion that feldspar thermometry can be a reliable method

683   for establishing temperatures of crystallization at low temperatures if other measures indicate

684   that the feldspars have preserved their original igneous compositions (London et al., 2020;

685   London, 2022).

686   **Glass Compositions**

687   Boundary layer pile-up refers to an increase in the concentration of an incompatible element

688   along a crystallization front that results when the rate of advance of the crystalline front exceeds

689   the rate at which the incompatible element can diffuse away from that interface to erase its

690   chemical activity gradient. Among the principal fluxing components of pegmatite-forming melts,

691   H and F exhibit high diffusivity in flux-rich melts at high temperature, whereas the diffusion

692   coefficient of B is orders of magnitude smaller, similar to that of Al, and P diffuses even more

693   slowly than Si (Wolf and London, 1994; London, 2009, 2015). Boundary layer pile-up among F,

694   B, Rb, and Cs has been documented previously in the low-temperature experiments with the

695   Macusani obsidian and other compositions (London, 1999; London and Morgan, 2012, 2017).

696   The most prominent features of the glasses in this study were their chemical gradients among

697   most components along the central length of the cores and across them, even at very low levels

698   of crystallization. In some profiles, F and B possessed steep exponential gradients (Figures 8b

699   and 13), in others they varied linearly along the entire length of a melt column (Figure 6b). The

700   widths and magnitudes of the boundary layer pile-up of B relative to F in Figure 13 can be

701   explained by the differences in their diffusivity. Phosphorus showed little variation in any

702   analytical profiles of the glass, even though its diffusivity in granitic melt is exceedingly low

703   (Wolf and London, 1994), and boundary-layer pile up of phosphorus is expected (e.g., Morgan

704   and London, 2005b). The lack of variation in phosphorus in these experiments arose from the

705   high ASI of the Macusani obsidian, which promoted the incorporation of P in alkali feldspars

706   (London et al., 1993) to the extent that the bulk distribution coefficient for P was approximately

707   unity (Electronic Appendix I).

708   The ratios of K and Na, expressed as K*, varied systematically along the lengths of the cores

709   such that values of K* were mostly antithetical to those of F (Figure 8b) and to Al and to ASI but

710   correlated positively with Si (Figure 6a). High concentrations of Na in glass (low values of K*)

711   occurred adjacent to plagioclase-rich crystallization fronts, and high K* values developed in

712   glass where mostly K-feldspar precipitated (Figure 12a). Normally, opposite gradients would

713   have been expected: a K-enriched melt adjacent to a plagioclase crystallization front, and an Na-

714   enriched melt adjacent to a K-feldspar-rich domain as a result of an accumulation of the

715   excluded elements, Na or K (e.g., see Figures 7 and 9 of London, 2009). Sodium, Al, and F were

716   positively correlated in the glass of segment 1 of MAC 247 (Figure 8). An association among

Revision 1

717   Na, Al, and F as a cryolite (Na_3AlF_6) component in melt has been noted from other experiments

718   (e.g., Manning, 1981), and cryolite was observed as inclusions within quartz that crystallized

719   from the Macusani obsidian melt (Figure 14 of London, 2014). London (2014) explained the

720   cryolite as a precipitate from a boundary layer liquid because the bulk melt was undersaturated

721   with respect to cryolite.

722   Growth steps that are evident in large, tapering crystals from pegmatites appear to result from

723   cyclical episodes of crystallization (e.g., Figure 17-4 of London, 2008). The consequence of

724   episodic growth is that abrupt boundary layer pile-up of incompatible elements in the melt

725   adjacent to crystals would be erased over the interval of time in which growth has ceased, and

726   diffusion would erase those gradients completely if no further crystallization ensued. In a time

727   series of experiments, the chemical gradients in glass would therefore be transient as a function

728   of the timing of quench in relation to the burst of crystallization.

729   The antithetical gradients between Si and Al that are evident along the cores of MAC 246 and

730   MAC 247, however, are not likely the result of crystallization for the reasons that the proportion

731   of crystallization was too low to affect the two most abundant cationic components of the melt,

732   and the diffusivities of these components are exceedingly low even at the high temperatures

733   (800°C) at which they have been measured (e.g., Acosta-Vigil et al., 2012). London (2009)

734   observed, however, that gradients in slow-diffusing ions can be modified quickly by the

735   diffusion of other components. In the experiments described in London (2009), the diffusion of

736   alkalis, F, and B erased a chemical gradient of Si in the melt at a rate that was orders of

737   magnitude faster than the rate at which Si diffused away from crystals of quartz as they dissolved

738   into the melt. In MAC 246 and MAC 247, chemical gradients of Si and Al were created,

739   however, not erased. It is possible, therefore, that the concentration profiles of Si and Al reflect a

Revision 1

740   reorganization of the melts in response to the temperature gradients, such that Al and its charge-

741   balancing Na were concentrated at the cold ends of the melt columns, leaving Si and K enriched

742   in the opposite direction. Such variations, however, appear to be small in relation to the chemical

743   gradients in melt caused by crystallization.

744   Like MAC 246 and MAC 247, the thermal gradient along MAC 244 should have simulated the

745   continuous cooling of half a dike, margin to center, with a decreasing fraction of crystals to melt

746   from the cold to the hot end. However, MAC 244 resembles the zonation that would be expected

747   across an entire dike: most crystallization occurred at both ends of the melt column and

748   decreased toward the center of the core (Figure 10). The textures at the hot end of MAC 244

749   were the similar to the border zone at the cold end of the core and along the margins (Figures

750   10a,d). MAC 244, therefore, apparently did not begin to crystallize at its hot end until it had

751   cooled into the low-temperature realm that produced the fine-grained textures of the other highly

752   undercooled experiments (London et al., 1989; London and Morgan, 2017). If that interpretation

753   is correct, then the result augments other evidence that the magnitude of liquidus undercooling is

754   more important to initiate crystallization in high-viscosity granitic melts than the rate at which it

755   is attained (London, 2008, 2014a, 2018).

756   **Implications of Liquidus Undercooling for the Crystallization of Granite-Pegmatite Melts**

757   London (2008) proposed that pegmatites are granitic in composition because the high viscosity

758   of their melts inhibits the nucleation of crystals until liquidus undercooling by 150°-250°C

759   (actual temperatures of ~ 400°-500°C) finally triggers the crystallization response. Pegmatitic

760   textures are the result of crystallization of highly viscous melt at the undercooled state far from

761   the equilibrium of the liquidus (London, 2008, 2014b). Mafic and alkaline melts, with their

762   higher temperatures and lower melt viscosities, nucleate crystals more readily near the liquidus

Revision 1

763   surface, and uniform textures and assemblages are the more common result. Now, however, the

764   resistance to crystallization shown by undercooled liquidus experiments with granitic and flux-

765   rich pegmatitic compositions poses a problem in relation to the modeled cooling histories of thin

766   granitic dikes emplaced into much cooler host rocks. According to the numerical simulations of

767   heat flow, a delay in crystal nucleation and growth by weeks to months would put the pegmatite-

768   forming melts well below their glass transition temperature by the time crystallization

769   commenced.

770   *Isothermal Powder Experiments*. The undercooled powder experiments with the Macusani

771   obsidian (London et al., 1989) were the first such results that replicated the essential aspects of

772   mineral zonation and texture in pegmatites. The increasing chemical fractionation of the H_2O-

773   undersaturated melt also followed a trajectory that would, in pegmatites, lead to the precipitation

774   of normally rare minerals. In that set of experiments, the sequence of crystallization in an

775   undercooled granitic melt that contained measurable Ca conformed to expectations based on the

776   calculated Gibbs Free Energy liberated by the feldspar- and quartz-forming components (Table

777   3).

778   *Isothermal Core Experiments*. London and Morgan (2017) documented the spatial separation of

779   plagioclase-quartz and K-feldspar-rich assemblages on opposite ends of the melt column when a

780   surface (powdered amphibolite) was present to initiate and localize the crystallization of

781   plagioclase plus quartz. The spatial segregation of feldspars is a key aspect of zonation within

782   pegmatites (e.g., Jahns and Tuttle, 1963). Though plagioclase plus quartz were the first-formed

783   phases in the experiments, K-feldspar crystallized synchronously; thus, the actual mineral

784   assemblage was the ternary assemblage that would have been expected from a granitic liquid at

785   temperatures below the solidus and the solvus of the feldspar system. Feldspars were in chemical

Revision 1

786   and thermal equilibrium via the rapid diffusion of alkalis across the melt volume, which might

787   have been glass in experiments of 550°C and below, even at the highly undercooled and

788   metastable state of the glass. An aqueous solution played no part in the transfer of alkalis

789   between the end domains (cf. Jahns, 1982).

790   ***Polythermal Core Experiments***. The experiments presented here add a previously unseen

791   component to the crystallization response of the Macusani obsidian, that of repeated oscillations

792   of mineral phases from the margins to center of melt volumes and from cold to hot ends along

793   the lengths of melt columns. The normative compositions of the border and wall zones of MAC

794   244 are a near-exact replication of the same features in the Swamp dike (Figure 14), which is

795   typical of the more complexly zoned, subhorizontal, and layered pegmatites (Norton, 1983). The

796   comprehensive sequence of mineral assemblages in pegmatites – 11 such zones from margin to

797   center – is also characterized by oscillations in the abundances of plagioclase, K-feldspar, and

798   quartz that culminate in pure quartz that constitutes the pegmatite core (Table 1 of Cameron et

799   al., 1949).

800   The Macusani obsidian represents a close approximation to the compositions of highly

801   fractionated lithium-rich pegmatites, but these constitute far less than 1% of all pegmatites

802   (Černý, 1991). Otherwise, the compositions of pegmatites lie close to the thermal minimum in

803   the granite system, they lack exotic mineralogy, they are non-miarolitic, and they have not

804   generated metasomatic or other contact aureoles in their host rocks. Experiments likes the ones

805   presented here with compositions closer to the simple hydrous haplogranite minimum would be

806   more representative of pegmatites, but reverse-direction undercooled liquidus experiments

807   starting with solid glass cores of that composition do not crystallize in a time frame on which

808   academic geoscientists might be willing to stake their careers. Successful and complete

Revision 1

809   crystallization experiments that employ hydrous haplogranite glass cores would likely run into

810   many months or years.

811   Experimental simulations are not the ultimate means of understanding pegmatites, merely an

812   addition to the body of knowledge that comes from more traditional petrologic studies of the real

813   things. Nonetheless, the experimental crystallization of undercooled melts derived from the

814   Macusani obsidian has consistently produced textural attributes, mineral zoning, and chemical

815   fractionation trends that are the same as those found in natural pegmatites.

823   **References**

824   Acosta-Vigil, A., London, D., and Morgan, G.B. VI (2012) Chemical diffusion of major and

825   minor components in granitic liquids: implications for the rates of homogenization of crustal

826   melts. Lithos, 153, 308-323.

827   Bowen, N.L. (1913) The melting phenomena of the plagioclase feldspars. American Journal of

828   Science, 210, 577-599.

829   Bowen, N.L. (1928) The evolution of the igneous rocks. Princeton University Press, Princeton,

830   NJ, 334 p.

37

Revision 1

831 Burnham, C.W. and Jahns, R.H. (1962) A method for determining the solubility of water in

832 silicate melts. American Journal of Science, 260, 721-745).

833 Cameron, E.N., Jahns, R.H., McNair, A.H., and Page, L.R. (1949) Internal structure of granitic

834 pegmatites. Economic Geology Monograph, 2, 115 p.

835 Černý, P. (1991) Rare-element granitic pegmatites, Part I: Anatomy and internal evolution of

836 pegmatite deposits. Geoscience Canada, (Ore Deposit Models series), 18, 49-67.

837 Černý, P. (2000) Constitution, petrology, affiliations and categories of miarolitic pegmatites. In:

838 Pezzotta, F. (Ed.), Mineralogy and petrology of shallow depth pegmatites. Memorie della

839 Società Italiana di Scienze Naturali e del Mueso Civico di Storia Naturale di Milano, 30, 5-12.

840 Devineau, K., Champallier, R., and Pichavant, M. (2020) Dynamic crystallization of a

841 haplogranitic melt: application to pegmatites. Journal of Petrology, 61, doi:

842 10.1093/petrology/egaa054.

843 Elkins, L.T. and Grove, T.L. (1990) Ternary feldspar experiments and thermodynamic models.

844 American Mineralogist, 75, 544-559.

845 Evensen, J.M. (2001) The geochemical budget of beryllium in silicic melts & superliquidus,

846 subliquidus, and starting state effects on the kinetics of crystallization in hydrous haplogranite

847 melts. Unpublished Ph.D. dissertation, University of Oklahoma, Norman, Oklahoma, 293 p.

848 Fenn, P.M. (1977) The nucleation and growth of alkali feldspars from hydrous melts. Canadian

849 Mineralogist, 15, 135-161.

850 Fenn, P.M. (1986) On the origin of graphic granite. American Mineralogist, 71, 325-330.

851 Fuhrman, M.L. and Lindsley, D.H. (1988) Ternary-feldspar modeling and thermometry.

852 American Mineralogist, 73, 201-215.

Revision 1

853   Heinrich, E.W. (1953) Zoning in pegmatite districts. American Mineralogist, 38, 68-87.

854   Jahns, R.H. (1953a) The genesis of pegmatites. I. Occurrence and origin of giant crystals.

855   American Mineralogist 38, 563-598.

856   Jahns, R.H. (1953b) The genesis of pegmatites. II. Quantitative analysis of lithium bearing

857   pegmatite, Mora County, New Mexico. American Mineralogist, 38, 1078-1112.

858   Jahns, R.H. (1982) Internal evolution of pegmatite bodies. In: Černý, P. (Ed.) Granitic

859   Pegmatites in Science and Industry. Mineralogical Association of Canada Short Course

860   Handbook, 8, 293-327.

861   Jahns and Burnham (1969) Experimental studies of pegmatite genesis: I. A model for the

862   derivation and crystallization of granitic pegmatites. Economic Geology and the Bulletin of

863   the Society of Economic Geologists, 64, 843-864.

864   Jahns, R.H. and Ewing, R.C. (1977) The Harding Mine, Taos County, New Mexico.

865   Mineralogical Record, 8, 115-126.

866   Jahns, R.H. and Tuttle, O.F. (1963) Layered pegmatite-aplite intrusives. Mineralogical Society of

867   America Special Paper, 1, 78-92.

868   London, D. (1999) Melt boundary layers and the growth of pegmatitic textures. (abstr.) Canadian

869   Mineralogist, 37, 826-827.

870   London, D. (1992) The application of experimental petrology to the genesis and crystallization

871   of granitic pegmatites. Canadian Mineralogist, 30, 499-540.

872   London, D. (2008) Pegmatites. Canadian Mineralogist Special Publication 10, 347 p.

873   London, D. (2009) The origin of primary textures in granitic pegmatites. Canadian Mineralogist,

874   47, 697-724.

875   London, D. (2013) Crystal-filled cavities in granitic pegmatites: bursting the bubble. Rocks &

876   Minerals, 88, 527-534.

877   London, D. (2014a) A petrologic assessment of internal zonation in granitic pegmatites. Lithos,

878   184-187, 74-104.

879   London, D. (2014b) Subsolidus isothermal fractional crystallization. American Mineralogist, 99,

880   543-546.

881   London, D. (2015) Erratum: The origin of primary textures in granitic pegmatites. Canadian

882   Mineralogist, 53, 591-592

883   London, D. (2018) Ore-forming processes within granitic pegmatites. Ore Geology Reviews,

884   101, 349-383

885   London, D. (2022) A Rayleigh model of cesium fractionation in granite-pegmatite systems.

886   American Mineralogist, 107, 82-91.

887   London, D., Hervig, R.L., and Morgan, G.B., VI (1988) Melt-vapor solubilities and element

888   partitioning in peraluminous granite-pegmatite systems: Experimental results with Macusani

889   glass at 200 MPa. Contributions to Mineralogy and Petrology, 99, 360-373.

890   London, D., Hunt, L.E., Schwing, C.R., and Guttery, B.M. (2020) Feldspar thermometry in

891   pegmatites: truth and consequences. Contributions to Mineralogy and Petrology, 175,

892   https://doi.org/10.1007/s00410-019-1617-z.

893   London, D., Hunt, L.E., Duval, C.L. (2021) Temperatures and duration of crystallization in gem-

894   bearing granitic pegmatites. Lithos, 360-361, https://doi.org/10.1016/j.lithos.2020.105417.

Revision 1

895   London, D. and Morgan, G.B. VI (2012) The pegmatite puzzle. Elements, 8, 263–268.

896   London, D. and Morgan, G.B. VI (2017) Experimental crystallization of the Macusani obsidian,

897   with applications to lithium-rich granitic pegmatites. Journal of Petrology, 58, 1005–1030.

898   London, D., Morgan, G.B. VI, and Acosta-Vigil, A. (2012a) Experimental simulations of

899   anatexis and assimilation involving metapelite and granitic melt. Lithos, 153, 292–307.

900   London, D., Morgan, G.B. VI, Paul, K.A., and Guttery, B.M. (2012b) Internal evolution of a

901   miarolitic granitic pegmatite: the Little Three Mine, Ramona, California (USA). Canadian

902   Mineralogist, 50, 1025-1054.

903   London, D., Morgan, G.B., VI, and Hervig, R.L. (1989) Vapor-undersaturated experiments in the

904   system macusanite-H_2O at 200 MPa, and the internal differentiation of granitic pegmatites.

905   Contributions to Mineralogy and Petrology, 102, 1-17

906   London, D., Morgan, G.B., VI, Babb, H.A., and Loomis, J.L. (1993) Behavior and effects of

907   phosphorus in the system Na_2O-K_2O-Al_2O_3-SiO_2-P_2O_5-H_2O at 200 MPa (H_2O). Contributions

908   to Mineralogy and Petrology, 113, 450-465.

909   Manning, D.A.C. (1981) The effect of fluorine on liquidus phase relationships in the system Qz-

910   Ab-Or with excess water at 1 kb. Contributions to Mineralogy and Petrology, 76, 206-215.

911   Moore, G., Righter, K., and Carmichael, I.S.E. (1995) The effect of dissolved water on the

912   oxidation state of iron in natural silicate liquids. Contributions to Mineralogy and Petrology,

913   120, 170-179, 1995.

914   Morgan G.B. VI (2015) Practical aspects of electron probe analysis of boron using a LSM device

915   with large 2d (abstr.). Microscopy and Microanalysis, 2015, #1141.

Revision 1

916   Morgan, G.B. VI & London, D. (1996) Optimizing the electron microprobe analysis of hydrous

917   alkali aluminosilicate glasses. American Mineralogist, 81, 1176-1185.

918   Morgan, G.B. VI & London, D. (2005a) Effect of current density on the electron microprobe

919   analysis of alkali aluminosilicate glasses. American Mineralogist 90, 1131-1138.

920   Morgan, G.B. VI and London, D. (2005b) Phosphorus distribution between potassic alkali

921   feldspar and metaluminous haplogranite liquid at 200 MPa (H_2O): the effect of undercooling

922   on crystal-liquid systematics. Contributions to Mineralogy and Petrology, 150, 456-471.

923   Mysen, B.O., Yamashita, S., Chertkova, N. (2008) Solubility and solution mechanisms of NOH

924   volatiles in silicate melts at high pressure and temperature: amine groups and hydrogen

925   fugacity. American Mineralogist, 93, 1760–1770.

926   Norton, J.J. (1966) Ternary diagrams of the quartz-feldspar content of pegmatites in Colorado.

927   U.S. Geological Survey Bulletin, 1241, D1-D16.

928   Norton, J.J. (1983) Sequence of mineral assemblages in differentiated granitic pegmatites.

929   Economic Geology, 78, 854-874.

930   Norton, J. J. and Redden, J. A. (1990) Relations of zoned pegmatites to other pegmatites, granite,

931   and metamorphic rocks in the southern Black Hills, South Dakota. American Mineralogist,

932   75, 631–655.

933   Parsons, I., Magee, C.W., Allen, C.M., Shelley, J.M.G., and Lee, M.R. (2009) Mutual

934   replacement reactions in alkali feldspars II: trace element partitioning and geothermometry.

935   Contributions to Mineralogy and Petrology, 157, 663–687.

Revision 1

936   Stilling, A., Černý, P., and Vanstone, P.J. (2006) The Tanco pegmatite at Bernic Lake, Manitoba.

937   XVI. Zonal and bulk compositions and their petrogenetic significance. Canadian

938   Mineralogist, 44, 599-623.

939   Swanson, S.E. (1977) Relation of nucleation and crystal-growth to the development of granitic

940   textures. American Mineralogist, 62, 966-978.

941   Taylor, J. R. and Wall, V. J. (1992) The behaviour of tin in granitoid magmas. Economic

942   Geology, 87, 403-420.

943   Tuttle, O.F. and Bowen, N.L. (1958) Origin of granite in the light of experimental studies in the

944   system $NaAlSi_3O_8$-$KAlSi_3O_8$-SiO_2-H_2O. Geological Society of America Memoir, 74, 153 p.

945   Wen, S. and Nekvasil, H. (1994) SOLVCAL: An interactive program package for calculating

946   ternary feldspar solvus and two-feldspar geothermometry. Computers & Geosciences, 20,

947   1025-1040.

948   Wolf, M.B. and London, D. (1994) Apatite dissolution into peraluminous haplogranitic melts: an

949   experimental study of solubilities and mechanisms. Geochimica et Cosmochimica Acta, 58,

950   4127-4145.

951   Wyllie, P.J. (1963) Applications of high pressure studies to the earth sciences. In High Pressure

952   Physics and Chemistry (Bradley, R.S., ed.), Academic Press, New York, 2, 1-89.

953   **Figures**

954   Figure 1. Phase boundary diagrams of temperature versus initial H_2O added for the Spruce Pine

955   pegmatite (in gray: Burnham and Nekvasil, 1986) and the Macusani obsidian (in black: London

956   et al., 1989). Black arrows denote the paths of liquidus undercooling of magnitude ΔT, followed

Revision 1

957   by increasing H_2O content of melt upon crystallization that ensued after an initial period of

958   nucleation delay.

959   Figure 2. Cooling history of MAC 244. Green line segments and squares denote temperatures

960   measured by the thermocouple near the cold end (Read T Cold) during the run. Blue line

961   segments and squares denote the approximate temperatures at the hot end (T Hot) based on prior

962   calibrations with the thermocouple at the location. Red line and squares (T Set) are temperature

963   settings on the controller.

964   Figure 3. Representative backscattered electron images with locations in MAC 246. Refer to the

965   text for explanations.

966   Figure 4. Convergent three-component (An-Ab-Or) temperatures (solid diamonds) derived from

967   the solvus thermometry program SOLVCAL against position within the experimental core. The

968   average temperatures among the three components that did not converge within the assigned

969   error in nine of the pairs analyzed are shown as gray squares. Other elements of the figure are

970   defined in the text.

971   Figure 5. Calculated temperatures and solvus boundaries versus the mole fractions of the

972   orthoclase component (X_{Or}) in plagioclase (Pl) and K-feldspar (Kfs) from MAC 246 for feldspars

973   that yielded a convergent temperature using the Margules mixing model of Elkins and Grove

974   (1991) as incorporated into SOLVCAL (Wen and Nekvasil, 1994).

975   Figure 6. Plots of chemical components of glass versus distance from the cold end of MAC 246.

976   ASI = molar Al/(Na+K+Ca); K* = molar K/(K+Na). Horizontal dashed lines convey the initial

977   concentration of each parameter in the Macusani obsidian with 5 wt.% added H_2O.

Revision 1

978   Figure 7. Representative backscattered electron images with locations in MAC 247. Refer to the

979   text for explanations.

980   Figure 8. Plots of chemical components of glass versus distance from the cold end of MAC 247.

981   ASI = molar Al/(Na+K+Ca); K* = molar K/(K+Na). Horizontal dashed lines convey the initial

982   concentration of each parameter in the Macusani obsidian with 5 wt.% added H_2O.

983   Figure 9. Representative backscattered electron images with locations in MAC 244. Refer to the

984   text for explanations. The ranges of temperatures reflect the initial and final temperatures at each

985   end of the core.

986   Figure 10. (a) A backscattered electron image toward the end of segment 6 at the hot end of

987   MAC 244 shows the spatial variations between K-feldspar and albite from margin to center and

988   with location along the length of the core. (b) A phase map at the end of segment 6 of MAC 244

989   that was constructed from co-added single-element x-ray maps. The phases are K-feldspar

990   (orange), albite (blue), quartz (green), mica (pink), apatite (yellow), and void (black).

991   Figure 11. Normative mineral variation diagrams along the length of the core for the border and

992   wall zones of the crystallization front, both scaled to a composite BSE image of the core. The

993   yellow line in segment 6 denotes a cross section of glass that was analyzed for Figure 13.

994   Figure 12. Plots of chemical attributes of the glass in MAC 244 along its length. ASI = molar

995   Al/(Na+K+Ca); K* = molar K/(K+Na). Horizontal dashed lines convey the initial concentration

996   of each parameter in the Macusani obsidian with 5 wt.% added H_2O.

997   Figure 13. Analyses of elements across glass of segment 6 of MAC 244, starting near a margin

998   dominated by K-feldspar and ending at the opposite margin that lacked crystallization. Refer to

999   the yellow line in Figure 10.

Revision 1

1000   Figure 14. Modal analysis by visual (1 square cm grid size) and microscopic point count (in

1001   aplite) across a complete dike cross section at the Little Three mine, Ramona, California, from

1002   London et al. (2012). Oscillations of mineral assemblages in the layered aplite are at a finer scale

1003   than the smoothed modal curves. Dark layers of aplite are mostly K-feldspar and tourmaline,

1004   light layers are plagioclase plus quartz.

1005   Figure 15. (a) Crystallization upward across a vertical section perpendicular to the contact of the

1006   footwall half of the Phantom dike, Little Three mine, Ramona, California (Figure 17-7 of

1007   London, 2008). The faint dark blue horizontal bands across the feldspars are phantom layers of

1008   fine-grained tourmaline that were deposited along the crystallization front. The texture of graphic

1009   granite (quartz-feldspar skeletal intergrowth) coarsened upward and separated into monophase

1010   domains at the top. (b) A cross section parallel to the contact across the same dike illustrates the

1011   fine-textured scale of the quartz intergrowth in Manebach twins of K-feldspar.

1012   **Tables**

1013   Table 1. Compositions of the Macusani Obsidian and the Tanco Pegmatite, Canada

1014   Table 2. Initial Experimental Conditions

1015   Table 3. Gibbs Free Energy Change at 500°C, 200 MPa, for crystallization from melt

1016
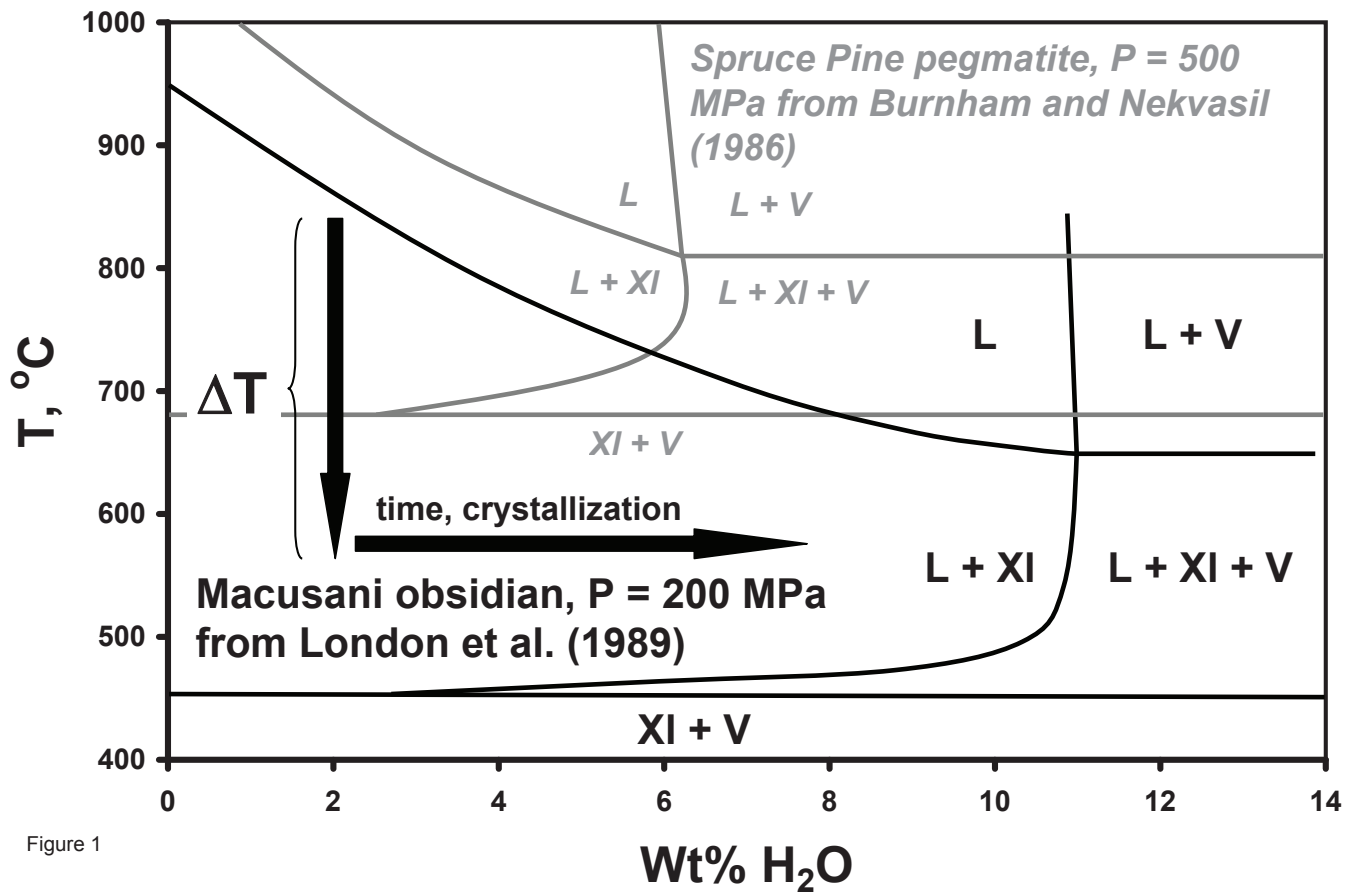
Figure 1

Figure 2

Figure 3

Fgure 4

MAC246

Figure 5

(a) Figure 6a

Figure 6b

Figure 7

(a)

Figure 8a

Chemical parameter
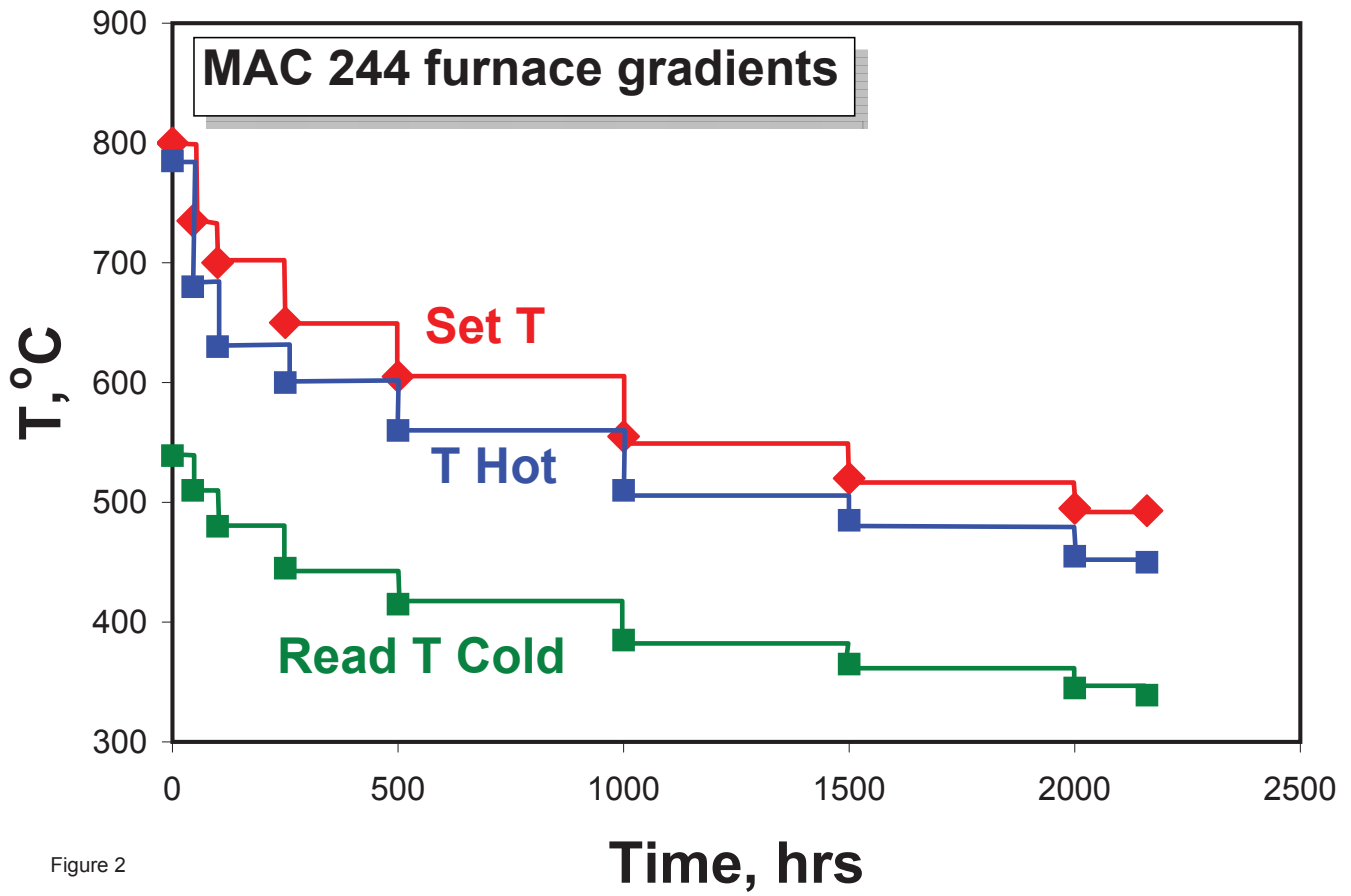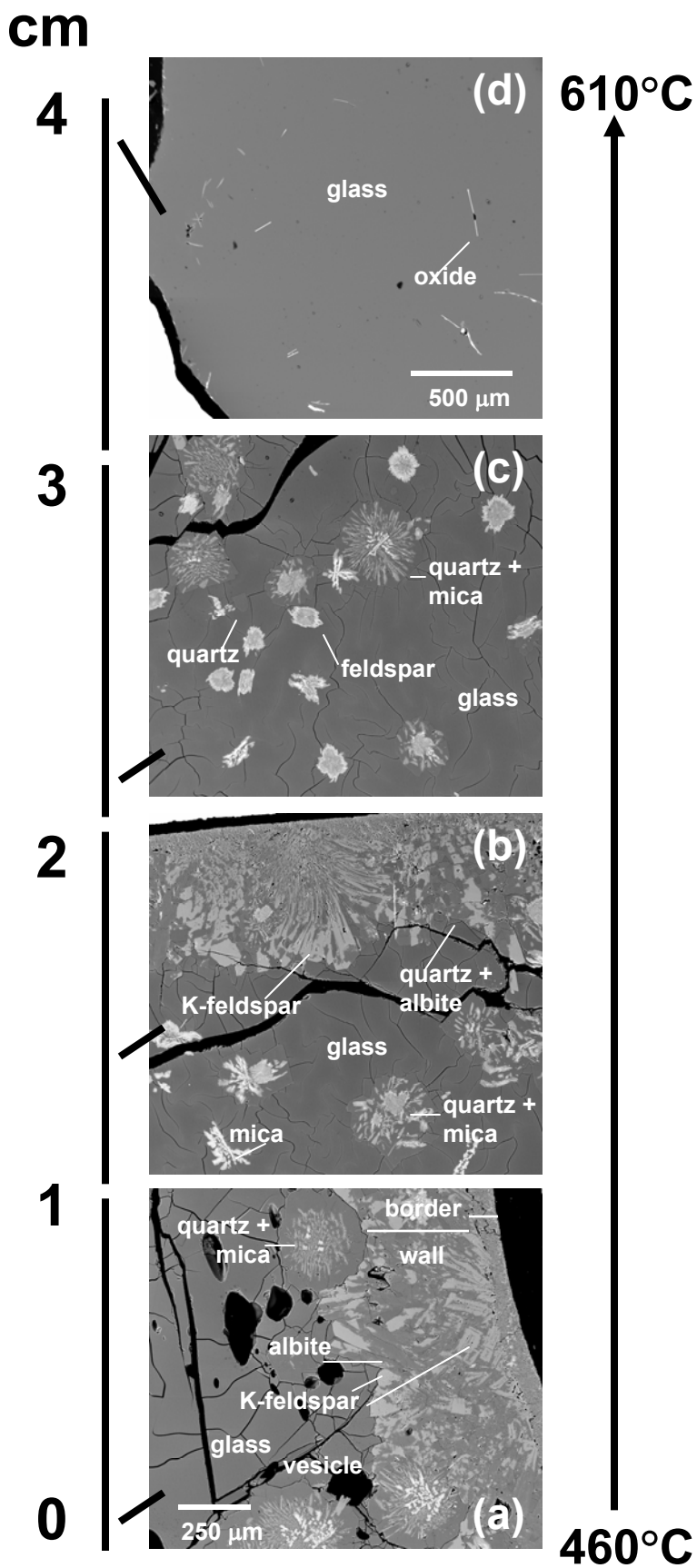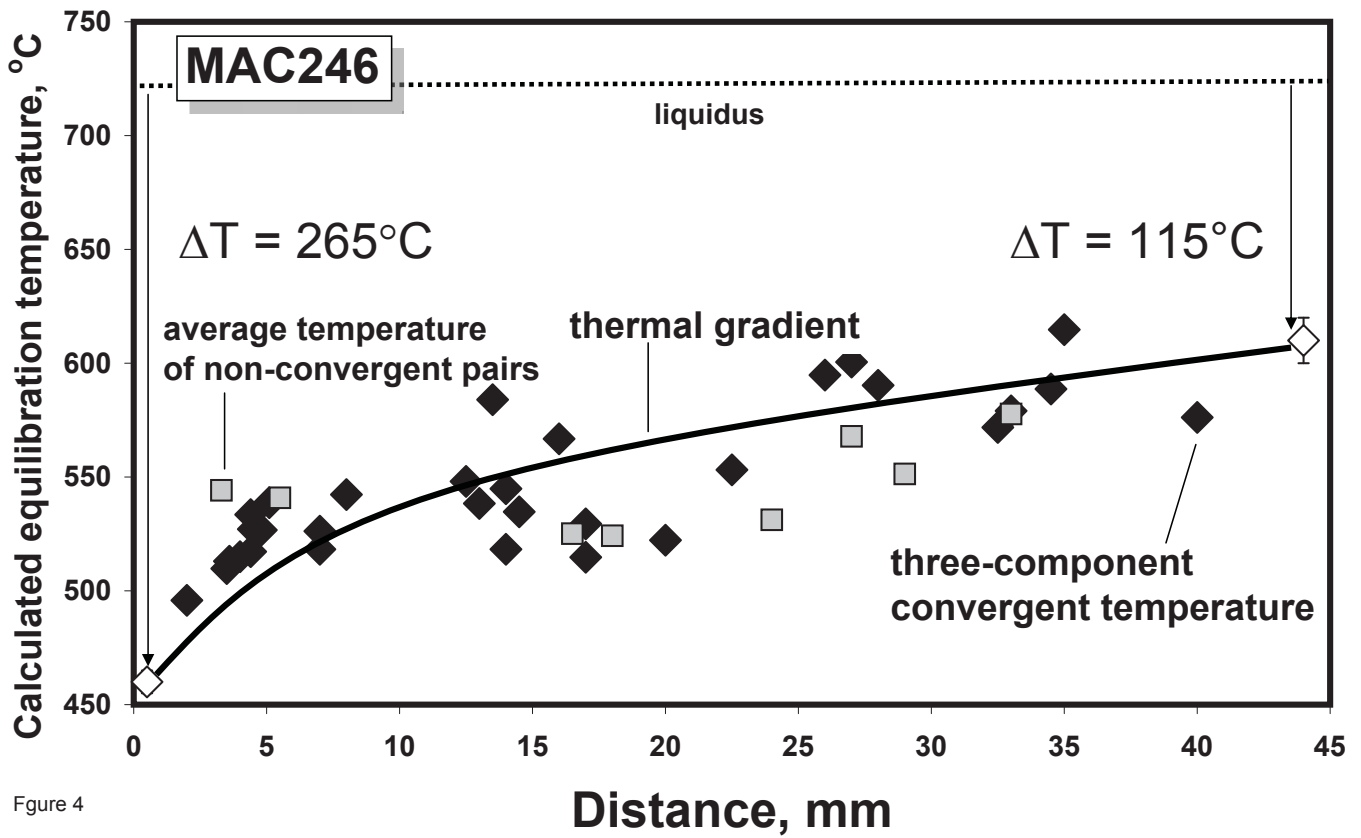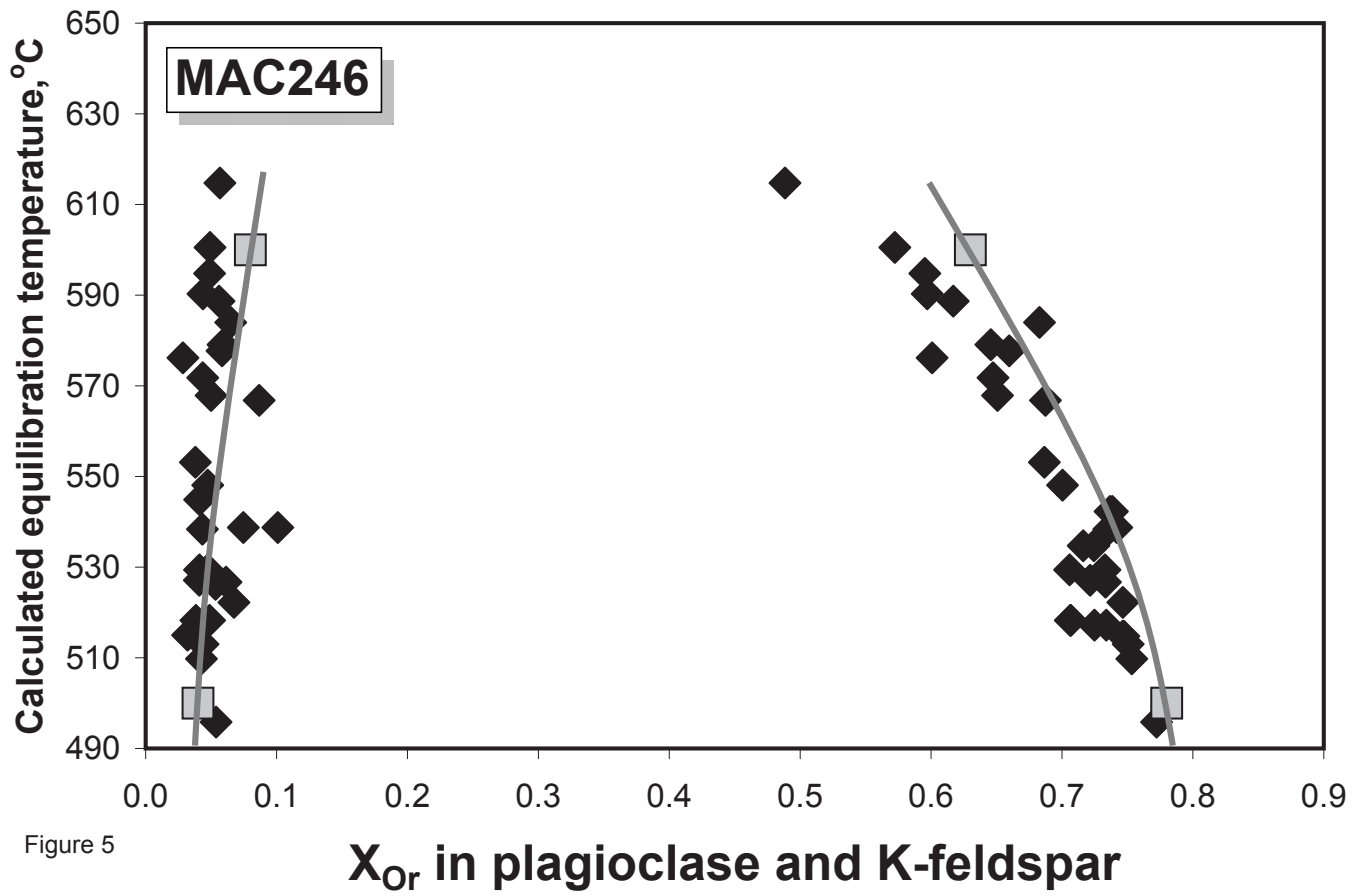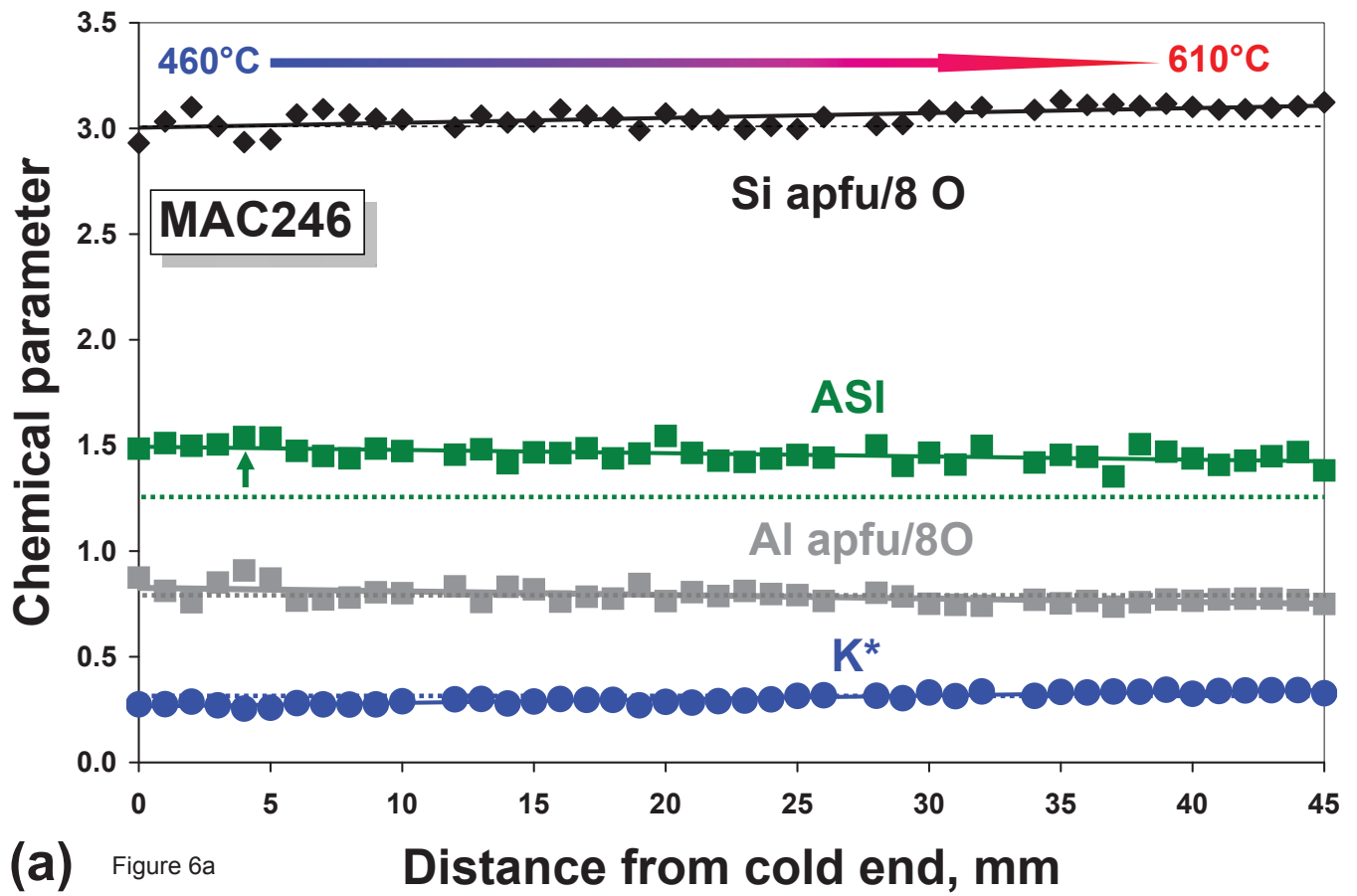
Distance from cold end, mm
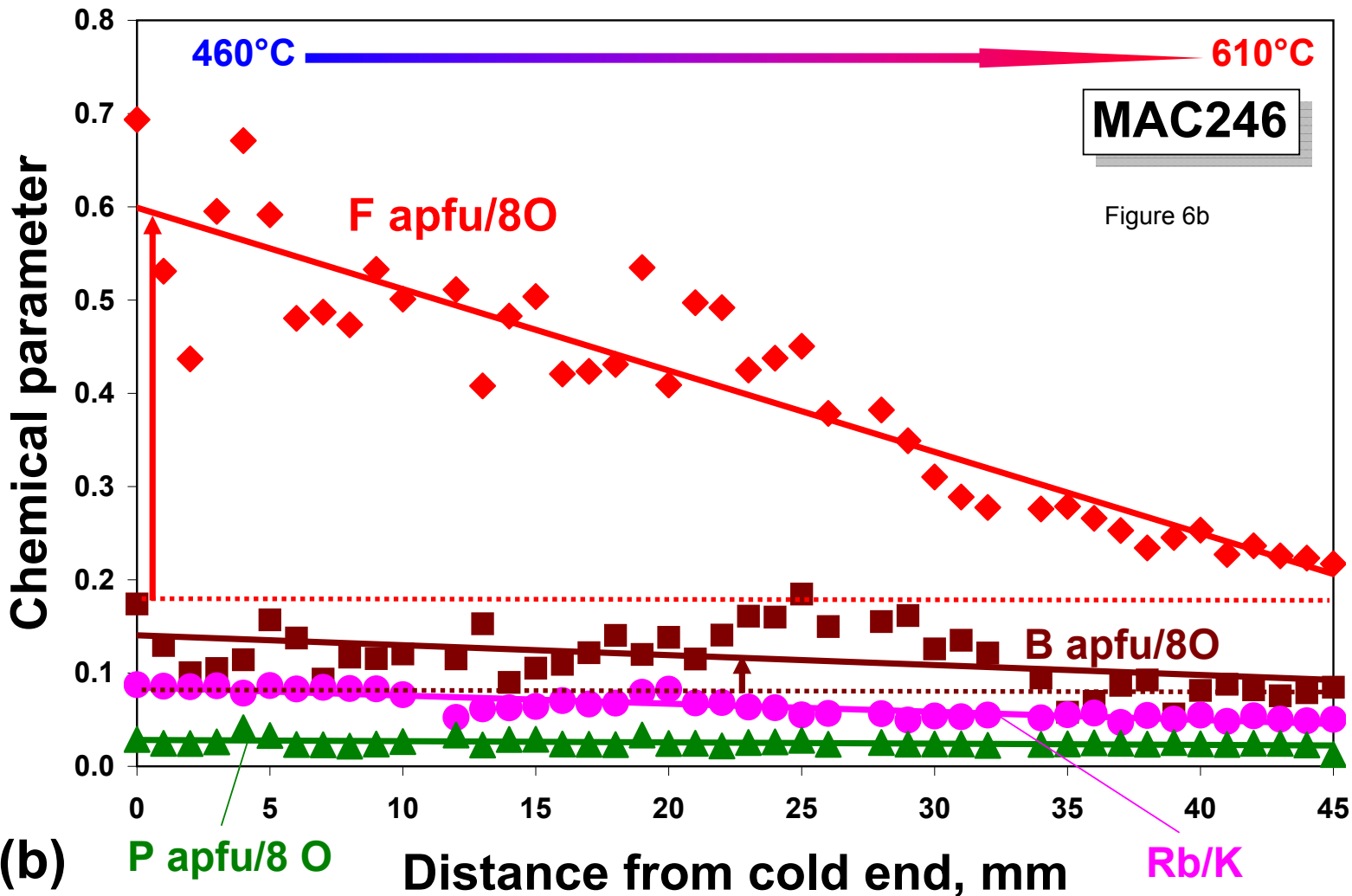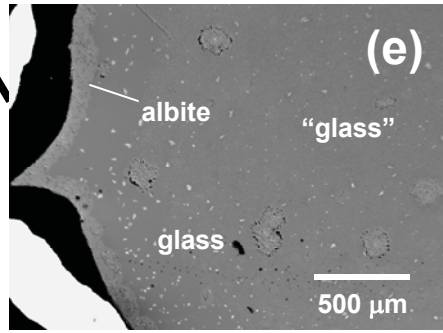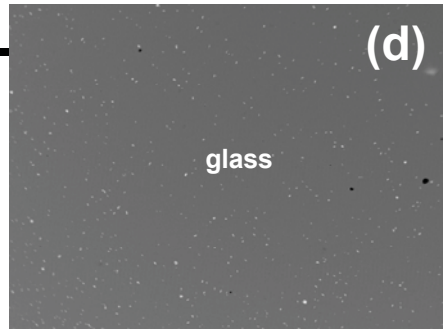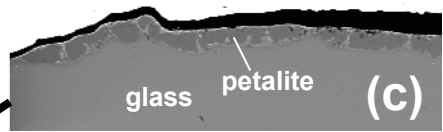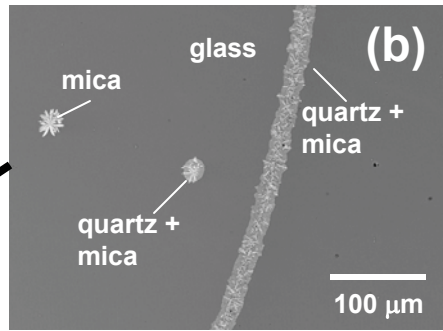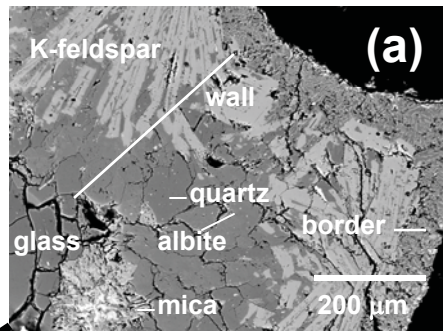
MAC247

Si apfu/8 O

410°C

585°C

ASI

Al apfu/8 O

(b) Figure 8b

Figure 9

(a) labels: K-feldspar, albite, glass + mica, 250 μm

(b) label: 100 μm

Figure 10

Figure 11

WALL
ZONE

Qz Or Ab

BORDER
ZONE

Qz Or Ab

0   30   60
Normative wt%

0   35   70
Normative wt%

(a) Figure 12a

(b) Figure 12b

Figure 13

Figure 14

Figure 15

TS#
6n
6m
6l
6k
6j
6i
4h
4g
4f
4e
4d
4c
4b
4a

Volume Fraction

0.00   0.20   0.40   0.60   0.80

56.3
53.1
49.9
46.6
43.3
40.1
36.8
33.6
30.3
27.1
23.8
20.6
17.3
14.1
10.8
7.5
4.3
1.1

Height (cm)

Qtz
Pl
Kfs
Trm
Ms
Gt
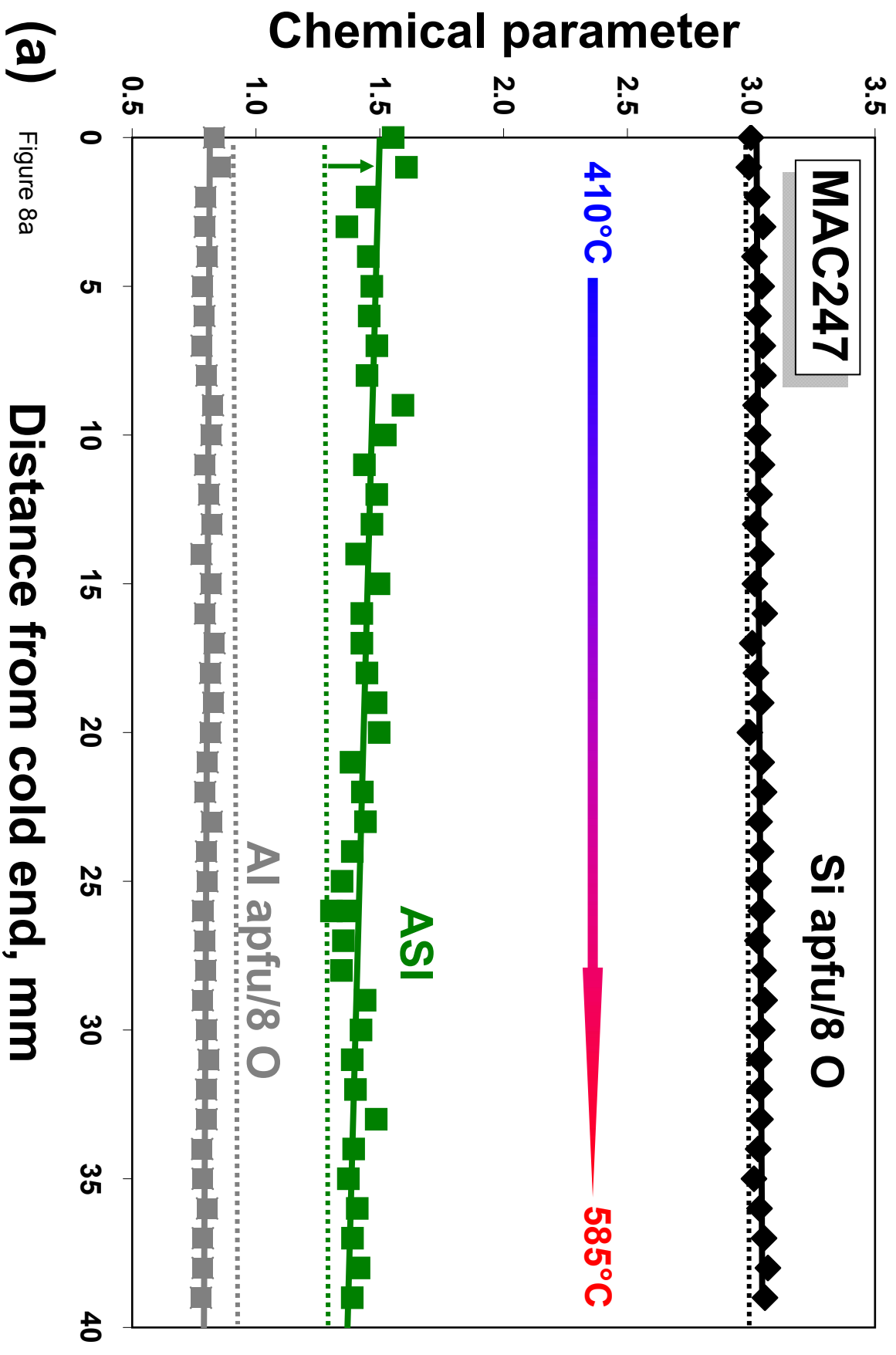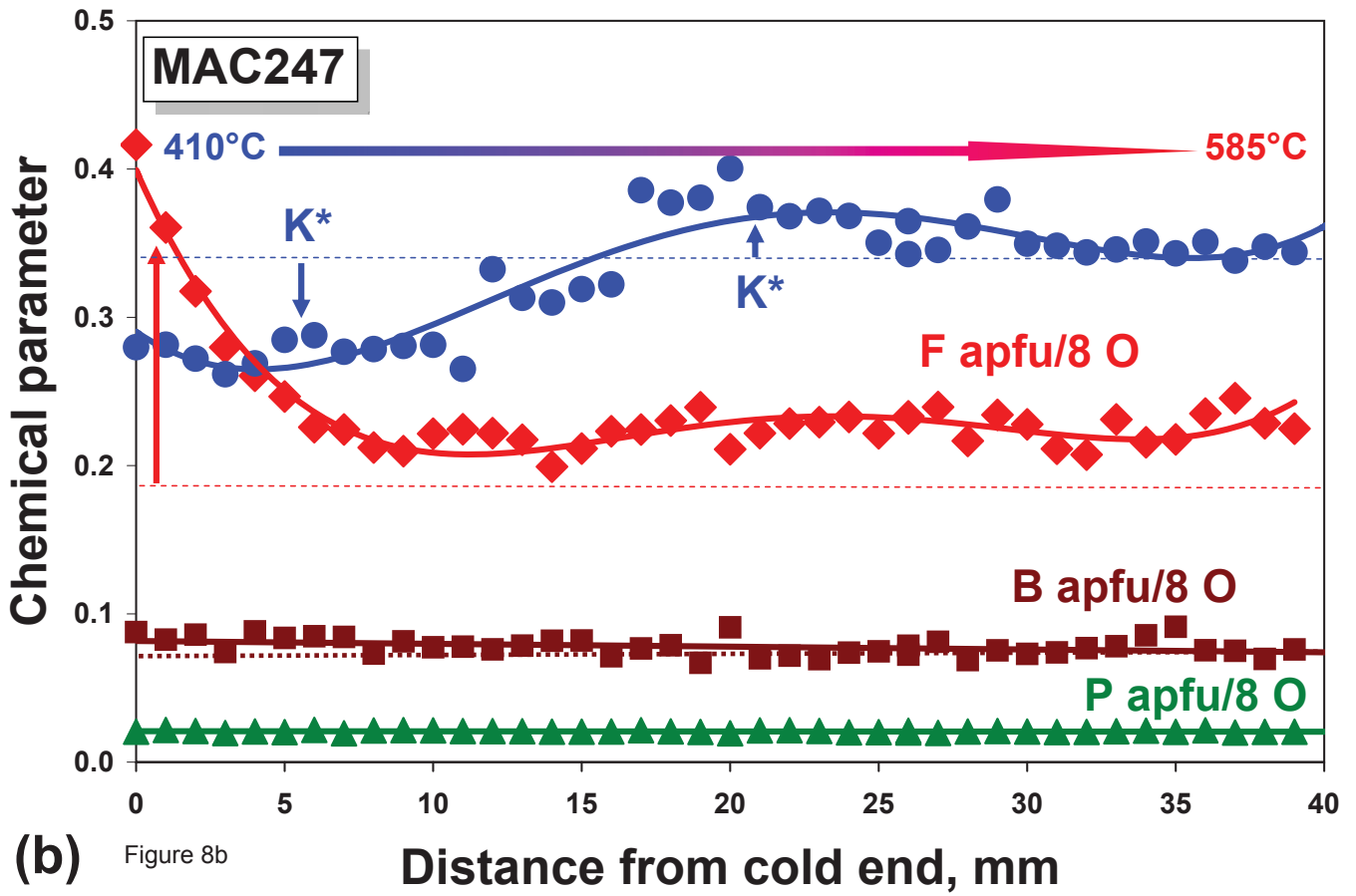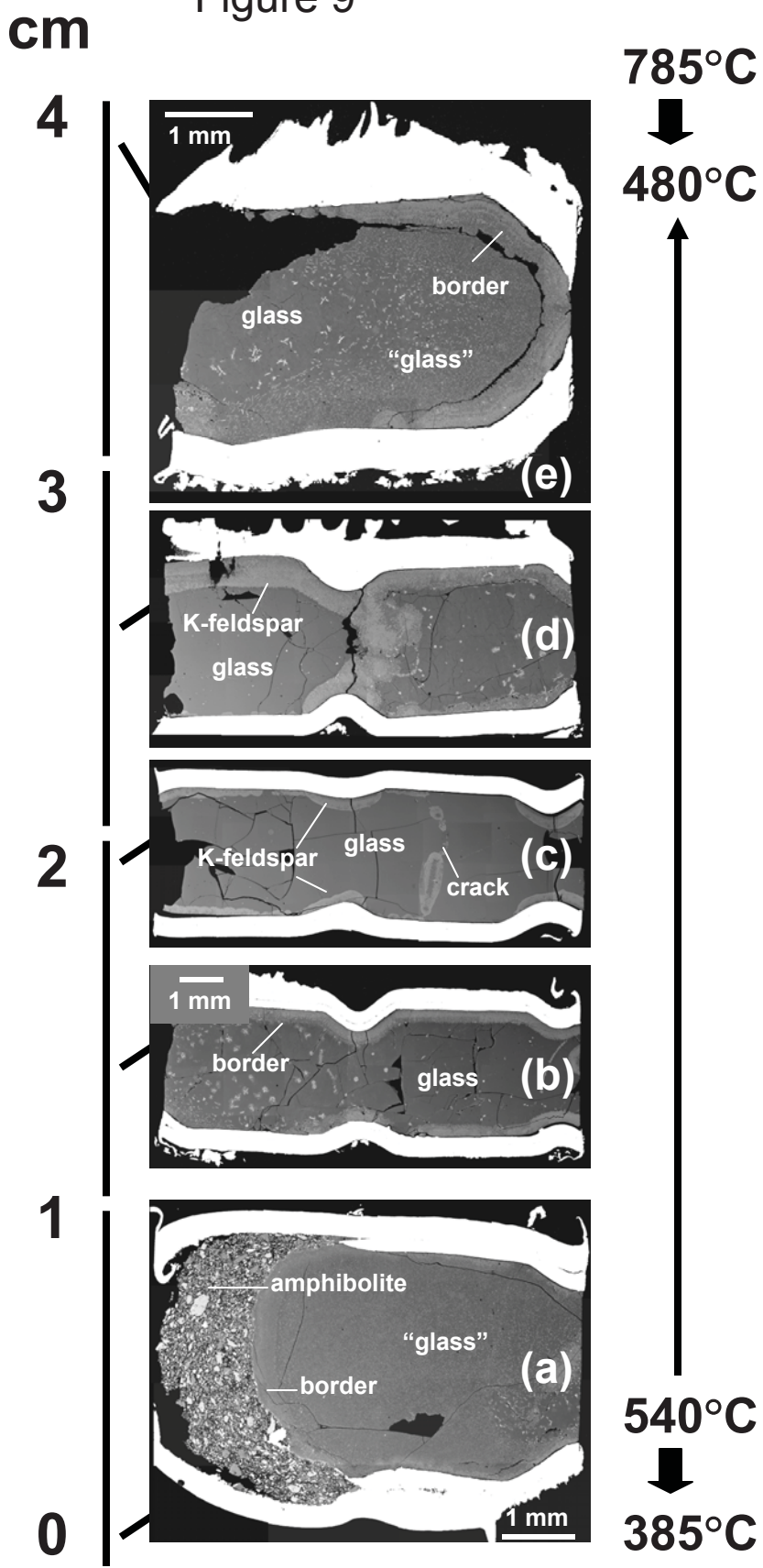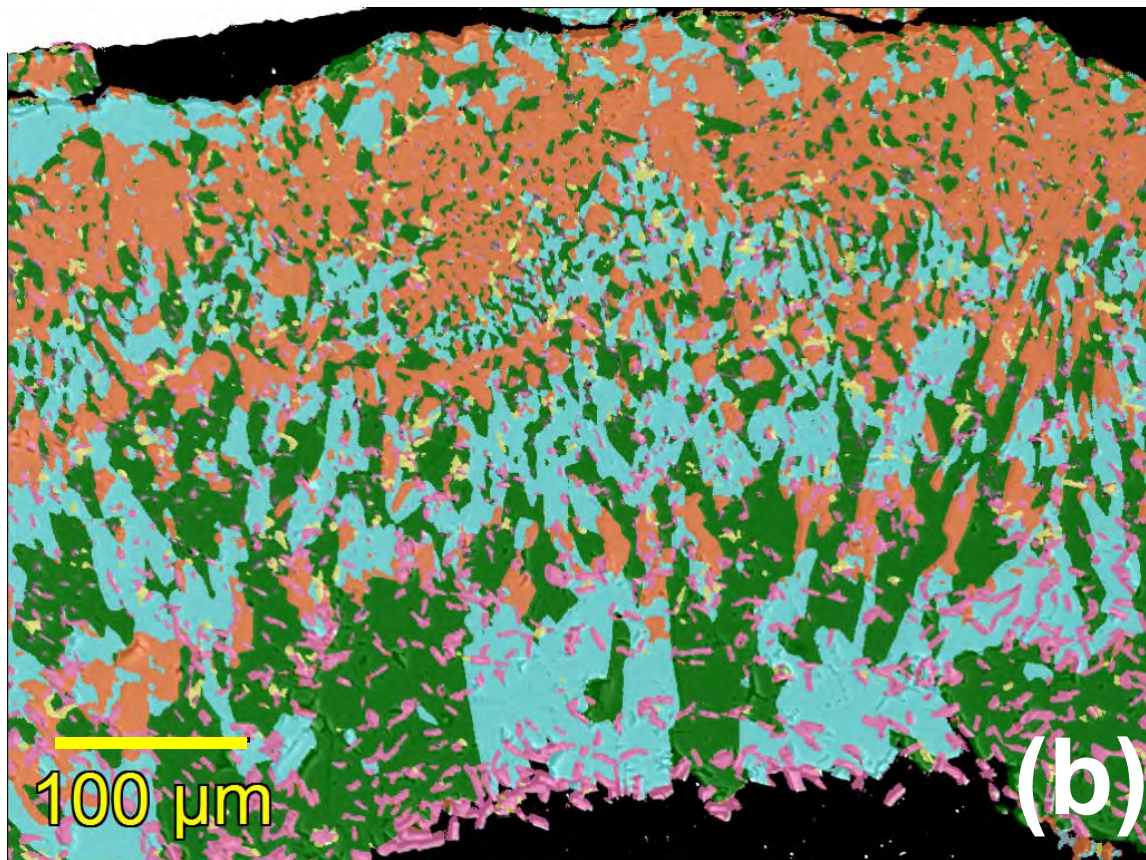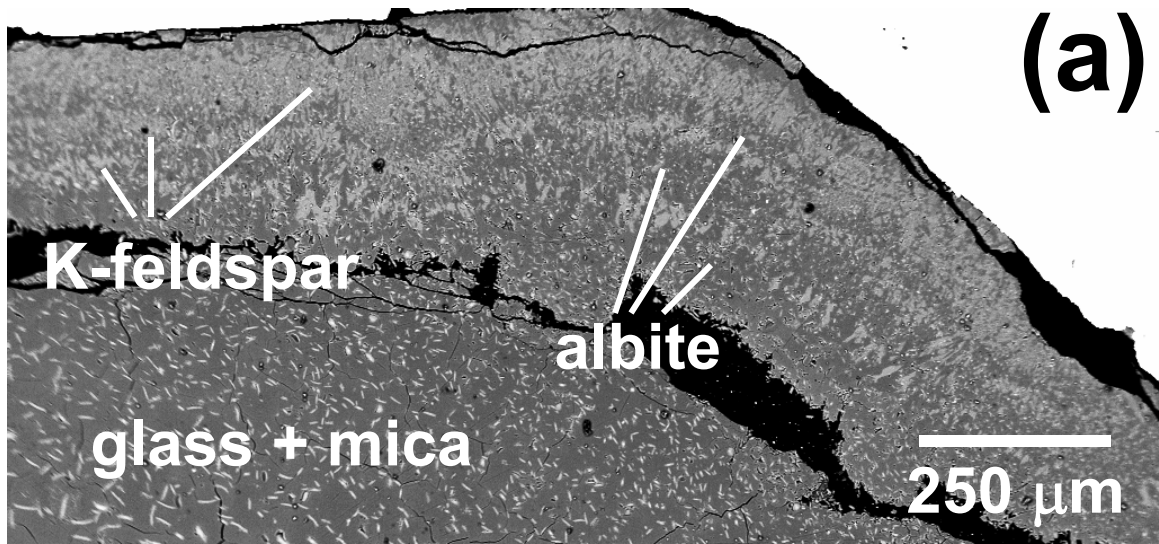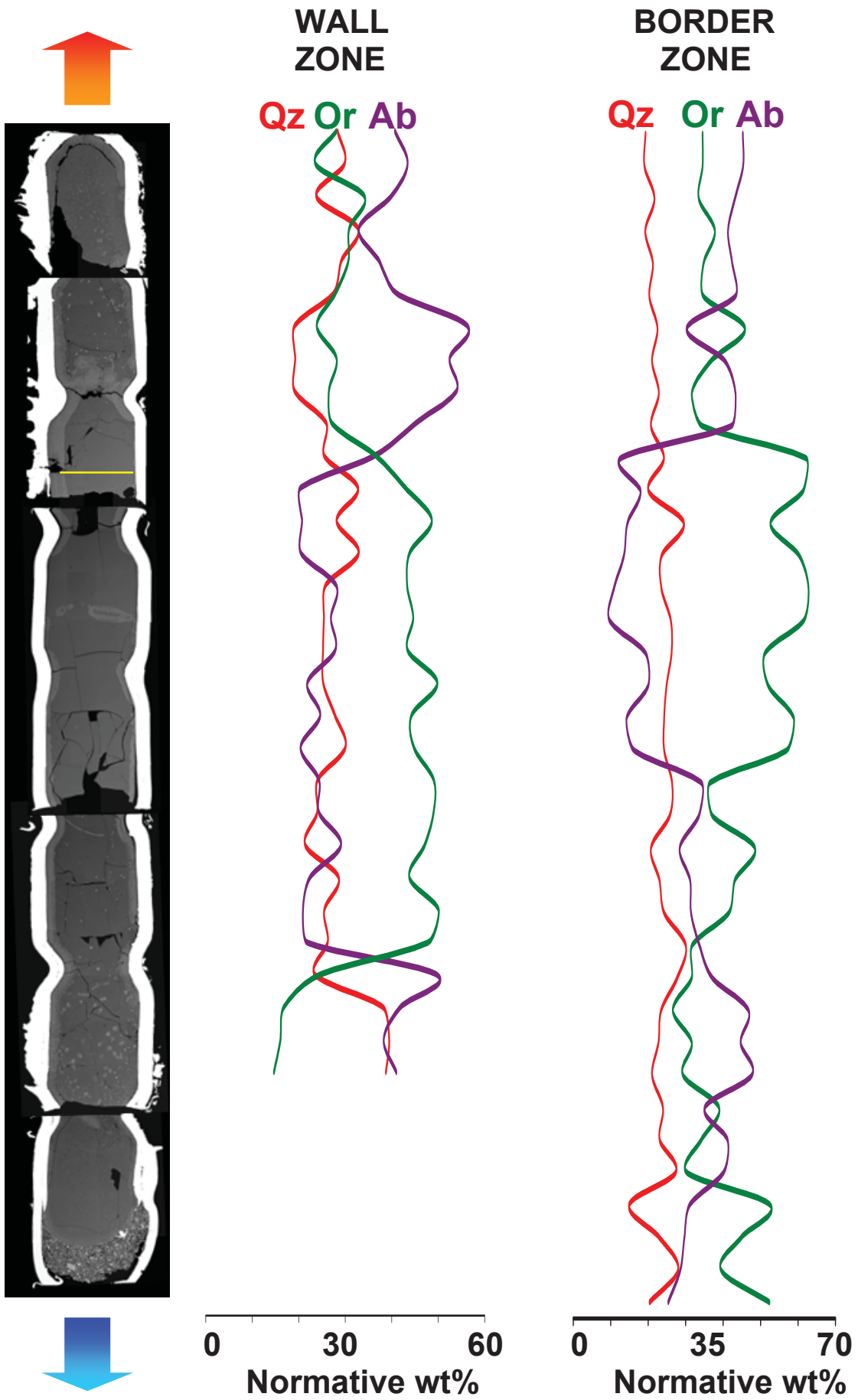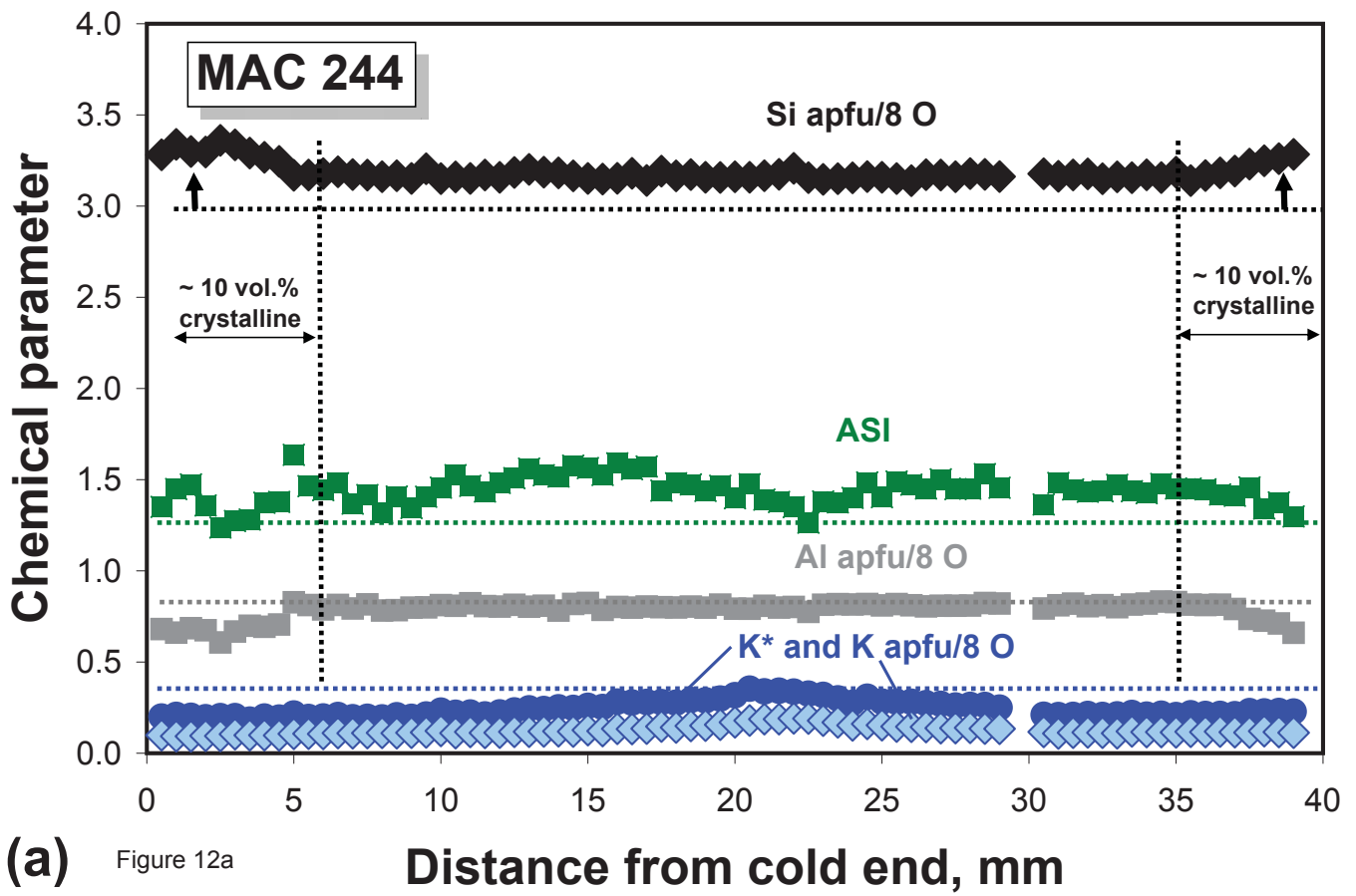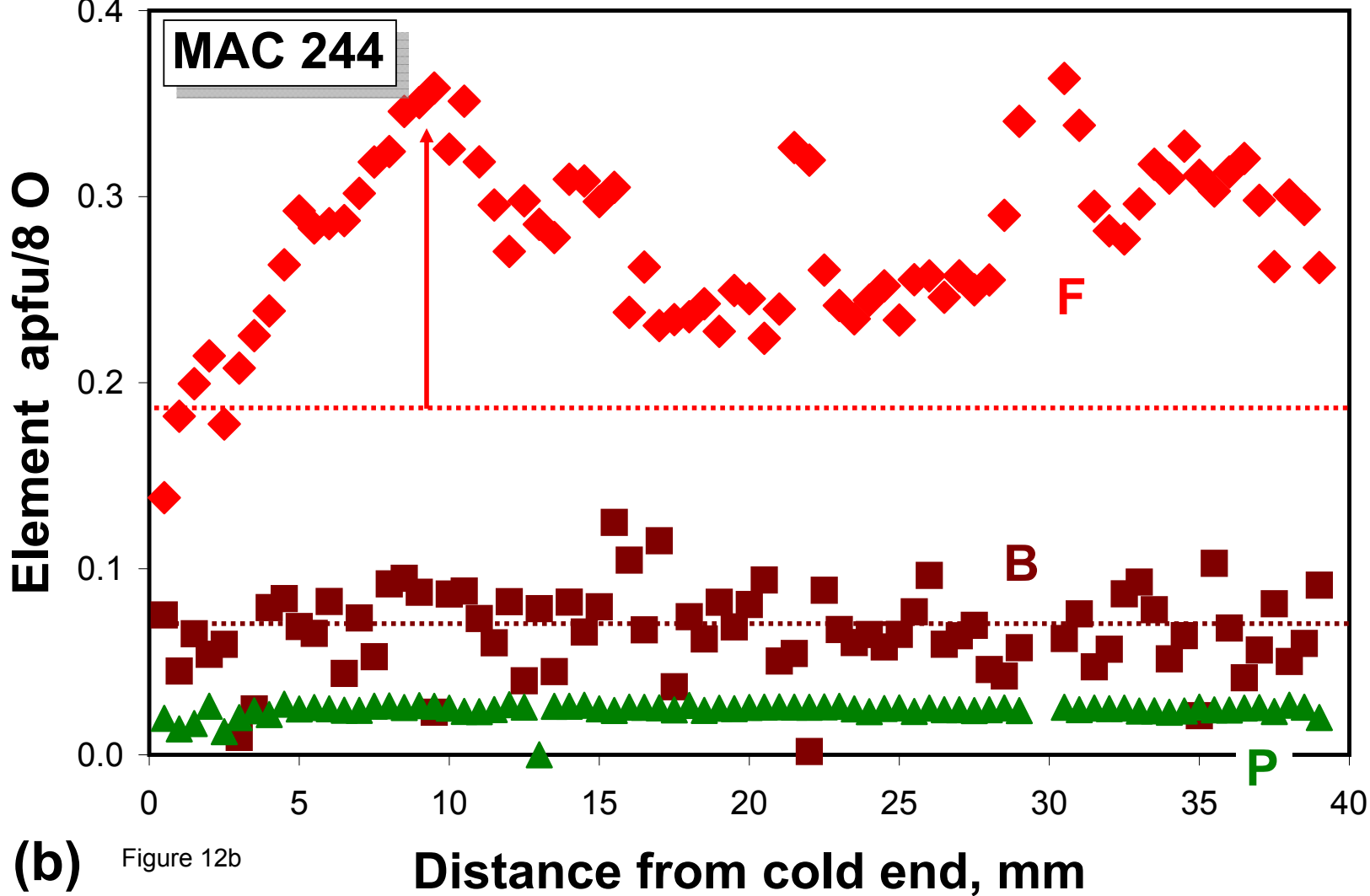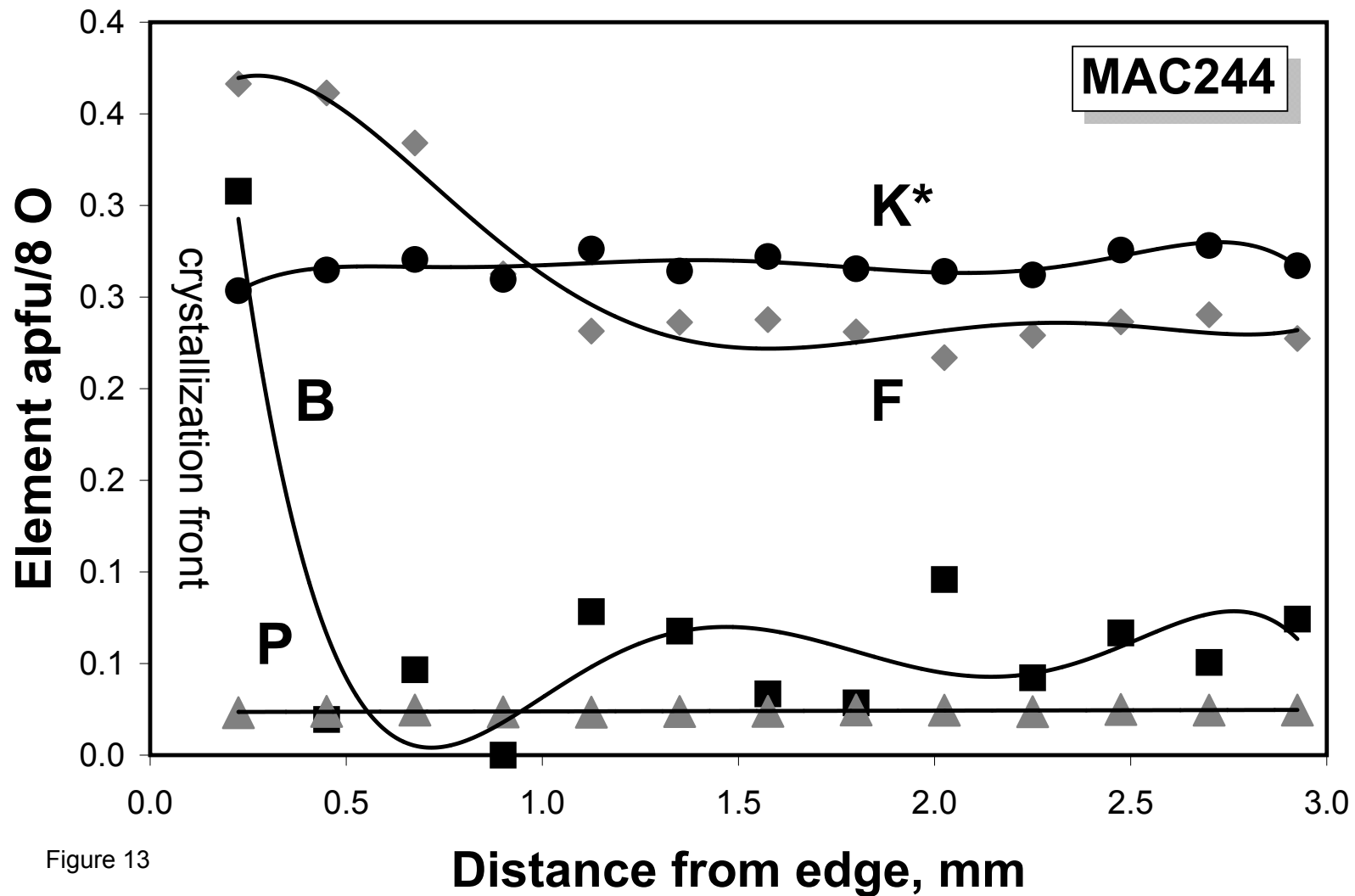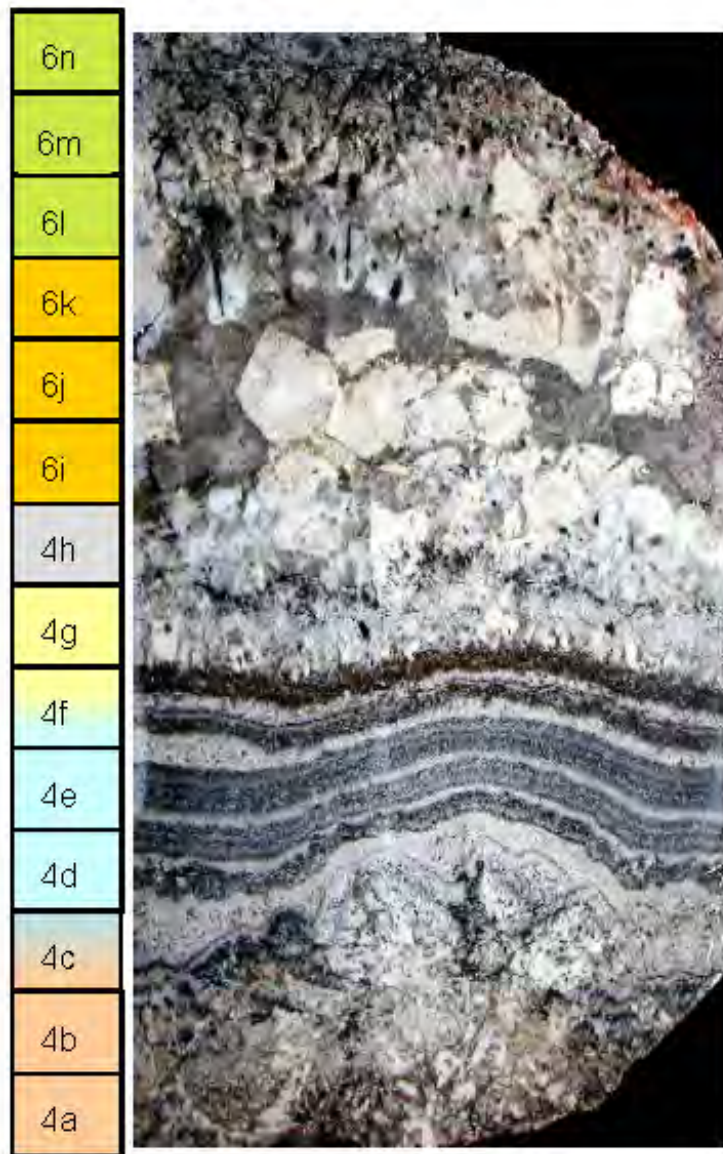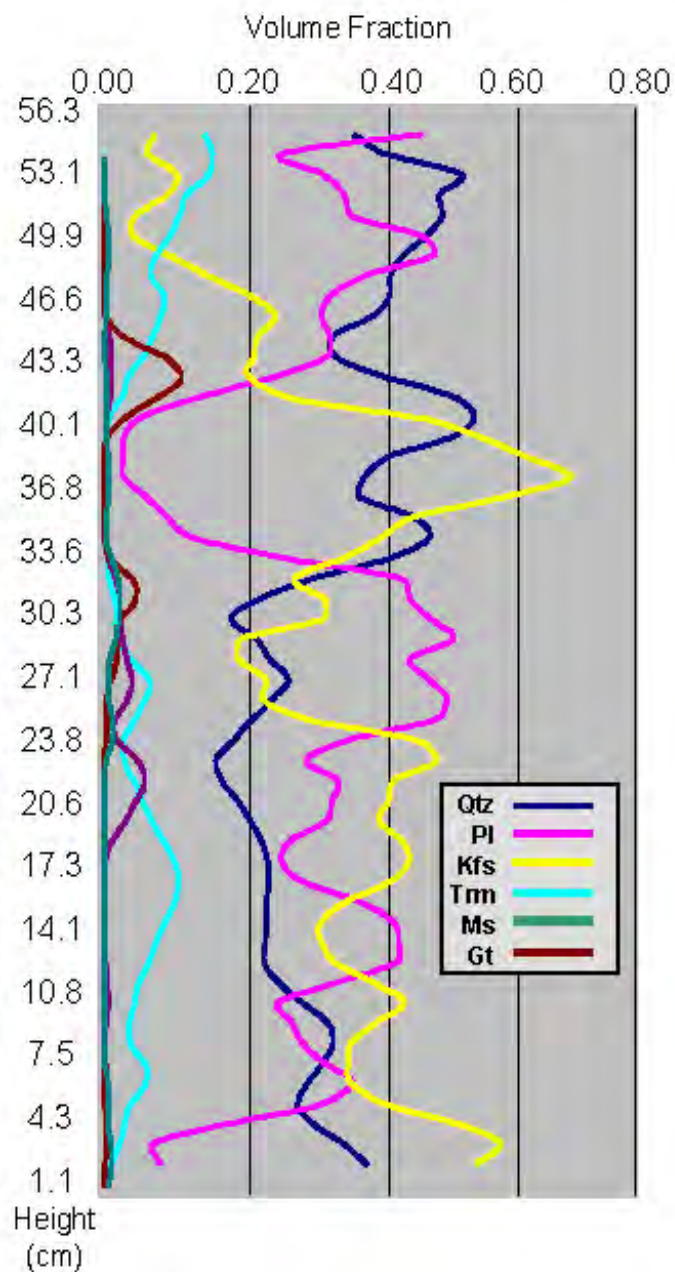
Figure 15
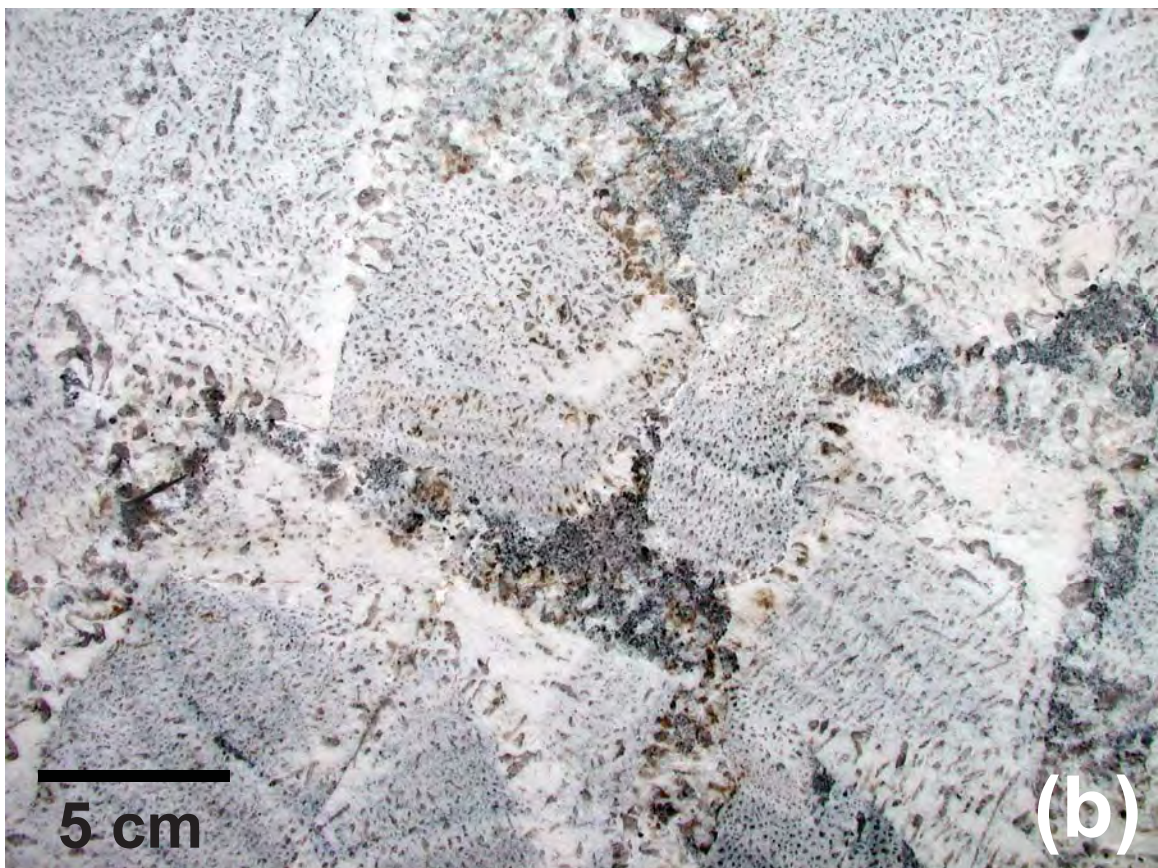
Table 1. Compositions of the Macusani Obsidian[1] and the Tanco Pegmatite[2], Canada

	Macusani	Tanco
oxide weight percent		
SiO_2	72.32	76.04
TiO_2	<0.02	0.01
Al_2O_3	15.63	13.62
Fe_2O_3	ND	0.01
FeO	0.52	0.15
MnO	<0.06	0.18
MgO	<0.02	0.01
CaO	0.23	0.15
BeO	0.00	0.05
Li_2O	0.16	0.76
Na_2O	4.10	4.10
K_2O	3.53	3.08
Rb_2O	0.11	0.60
Cs_2O	0.05	0.28
P_2O_5	0.58	0.86
B_2O_3	0.62	0.21
F	1.30	0.14
ppm		
Nb	51.3	55.79
Ta	24.1	299.73
Sn	200	71.38
ratios		
Nb/Ta	2.12	0.19
K*[3]	0.36	0.35
ASI[4]	1.41	1.06

[1] London et al. (1988)
[2] Stilling et al. (2006)
[3] mol K(K+Na)
[4] mol Al/(Li + Na + K + Rb + Cs + 2Ca)

Table 2. Initial Experimental Conditions

	H_2O wt.%	Cold °C	ΔT_{Cold} °C	Hot °C	ΔT_{Hot} °C	Duration, h
MAC 246	4.0	450	290	610	130	1,632
MAC 247	4.9	400	365	585	180	2,160
MAC 244	3.9	540	240	750	30	2,064

Table 3. Gibbs Free Energy Change at 500°C, 200 MPa, for crystallization from melt[1]

	ΔG, j/m
An	-50102
Ab	-23667
Or	-28086
Qz	-18586

[1] from equations in Table 1 and 2 of Burnham and Nekvasil (1986)